

## RESEARCH ARTICLE

10.1029/2019JC015090

## Key Points:

- This study represents the first 3-D Lagrangian evolution of Madagascar cyclonic eddies
- Madagascar cyclonic eddies transport approximately  $17.3 \pm 7.9$  Sv volume,  $-0.1 \pm 0.08$  PW heat and  $0.07 \pm 0.05$  Sv freshwater fluxes per eddy
- Ad hoc Argo experiments provide valuable insight in to the evolution of subsurface mesoscale eddy dynamics

## Correspondence to:

T. Morris,  
tamaryn.morris@weathersa.co.za

## Citation:

Morris, T., Aguiar-González, B., Ansoorge, I., & Hermes, J. (2019). Lagrangian evolution of two madagascar cyclonic eddies: Geometric properties, vertical structure, and fluxes. *Journal of Geophysical Research: Oceans*, 124, 8193–8218. <https://doi.org/10.1029/2019JC015090>

Received 24 FEB 2019

Accepted 13 OCT 2019

Accepted article online 2 NOV 2019

Published online 22 NOV 2019

## Lagrangian Evolution of Two Madagascar Cyclonic Eddies: Geometric Properties, Vertical Structure, and Fluxes

T. Morris<sup>1,2,3</sup> , B. Aguiar-González<sup>1,4,5</sup> , I. Ansoorge<sup>2</sup> , and J. Hermes<sup>1,2,6</sup> 

<sup>1</sup>Egagasini Node, South African Environmental Observation Network (SAEON), Cape Town, South Africa,

<sup>2</sup>Department of Oceanography, University of Cape Town (UCT), Cape Town, South Africa, <sup>3</sup>Now at Marine Unit, South African Weather Service (SAWS), Cape Town, South Africa, <sup>4</sup>Departamento de Física, Facultad de Ciencias del Mar, Universidad de Las Palmas de Gran Canaria, Las Palmas, Spain, <sup>5</sup>Royal Netherlands Institute for Sea Research (NIOZ), Department of Ocean Systems Sciences, and Utrecht University, Den Burg, Texel, The Netherlands, <sup>6</sup>Ocean Sciences Department, Nelson Mandela University (NMU), Port Elizabeth, South Africa

**Abstract** We investigate the 3-D Lagrangian evolution of two Madagascar cyclonic eddies based on ad hoc Argo experiments undertaken in April and July 2013. Eight Argo floats were configured to measure temperature and salinity at high temporal resolutions (daily and five-daily experiments) and varying park depths (300, 500, 650, and 1,000 m) to test their performance with regard to retention within the eddies described. Near-surface eddy properties are derived from an eddy detection and tracking algorithm applied to satellite altimetry data and a quasi eddy-resolving ( $1/4^\circ$ ) ocean general circulation model (GLORYS2v4). Both eddies propagated southwestward from southwest Madagascar ( $26^\circ\text{S}$ ,  $40^\circ\text{E}$ ), where the South East Madagascar Current separates from the continental shelf. During a travel of about 130 days at an average speed of  $11 \text{ km day}^{-1}$ , the eddies experienced well-defined growth, mature, and decay phases, interacting with the Agulhas Current at the KwaZulu-Natal Bight ( $28^\circ\text{S}$ ,  $34^\circ\text{E}$ ). Model-based estimates indicate the April (July) eddy showed mean trapping water depths of  $595 \pm 294 \text{ m}$  ( $914 \text{ m} \pm 107 \text{ m}$ ), volume transport about  $13.4 \pm 5.2 \text{ Sv}$  ( $21.2 \pm 9.1 \text{ Sv}$ ), heat flux of  $-0.07 \pm 0.06 \text{ PW}$  ( $-0.2 \pm 0.09 \text{ PW}$ ), and freshwater flux of  $0.04 \pm 0.04 \text{ Sv}$  ( $0.09 \pm 0.05 \text{ Sv}$ ). Peak estimates were found for both eddies during the mature eddy phase. These results highlight the role of Madagascar cyclonic eddies as transporters of cooled and freshened source waters into the Agulhas Current and illustrate the benefits of ad hoc Argo configurations for the study of 3-D Lagrangian eddy dynamics in combination with a “state-of-the-art” ocean model and remotely sensed data.

**Plain Language Summary** Mesoscale eddies formed south of Madagascar are normally shed as dipole structures, with a cyclonic eddy to the north and an anticyclonic eddy to the south, propagating westward toward the Agulhas Current. These features are generated at a frequency of four to six dipoles per year; however, these eddies interact with others traveling southward through the Mozambique Channel and westward from the Indian Ocean interior. This hampers our basic understanding of these features as nearly coherent entities feeding the Agulhas Current with source waters. We aim to provide a first description of the 3-D Lagrangian evolution of two Madagascar cyclonic eddies. Through the analyses of in situ and remotely sensed measurements, further complimented with numerical model data, a number of key features are revealed. The eddies propagated southwestward from  $26^\circ\text{S}$  at an average speed of  $11 \text{ km day}^{-1}$ . Their most important property is their capability to trap waters at their interior for a large vertical extent, thus becoming critical carriers of ocean properties toward the African coastline. We estimate the Madagascar cyclonic eddies of study transport  $17.3 \pm 7.9 \text{ Sv}$ , fluxing toward the Agulhas Current temperature and freshwater anomalies of  $-0.1 \pm 0.08 \text{ PW}$  (cooling) and  $0.07 \pm 0.05 \text{ Sv}$  (freshening), respectively.

### 1. Introduction

Mesoscale eddies are shed southwest off the southern tip of Madagascar (Figure 1), where the South East Madagascar Current (SEMC) detaches from the continental shelf and breaks up into a series of nearly symmetric dipolar vortex pairs at a frequency of four to six dipoles per year (Ridderinkhof et al., 2013). Based on

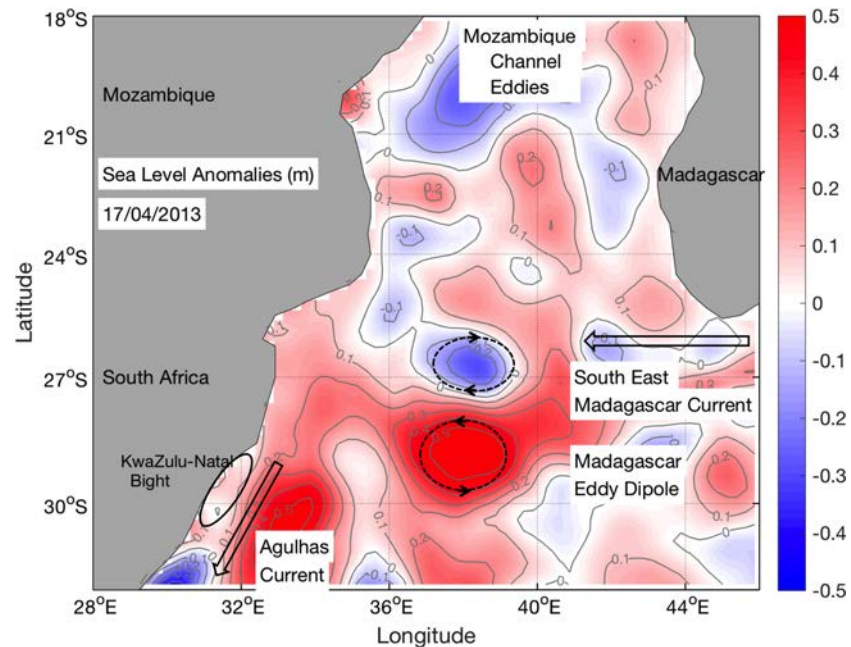


**Figure 1.** Map of sea level anomaly (m) of the southern Mozambique Channel for 17 April 2013 showing the contribution of mesoscale features in to the Agulhas Current. Major players are the southwestward eddy stream from the Mozambique Channel and the Madagascar eddy dipolar structure, formed off of the South East Madagascar Current (black arrow). Highlighted against the South African east coast is the location of the KwaZulu-Natal Bight (ellipse) and the Agulhas Current (black arrow). Positive (negative) sea level anomaly represented by red (blue) shaded contours is indicative of anticyclonic (cyclonic) geostrophic circulation.

model-based analyses of the energy conversion terms, Madagascar eddies have been suggested to be formed mainly in the upper ocean (0–300 m) by barotropic instability and at intermediate depths (800–2,000 m) by baroclinic instability (Halo, Penven, et al., 2014). These eddies tend to drift in a westward or southwestward direction across the southern Mozambique Channel (de Ruijter et al., 2004; Ridderinkhof et al., 2013) and interact with the southward eddy stream from the Mozambique Channel. Downstream, these eddies represent an important source of the flow and variability for the Agulhas Current (de Ruijter et al., 2004; Ridderinkhof et al., 2013; Schouten et al., 2002), the major western boundary current of the South Indian Ocean (Beal et al., 2011).

Previous studies on eddies in the southern Mozambique Channel have provided information about their mean size, amplitude, propagation speed, and seasonality (Halo, Penven, et al., 2014; Quartly et al., 2006; Siedler et al., 2009), yet a dedicated Lagrangian description of the eddy-driven volume, heat, and salt anomalies which ultimately impact the Agulhas Current remains missing in the literature. Mesoscale eddies can also trap and transport organic and inorganic materials over long distances when they exhibit nonlinear properties, that is, when the mean speed within the interior of the eddy or mean rotational speed exceeds the mean translation speed (Chelton et al., 2011; McWilliams & Flierl, 1979; Robinson, 1983). In line with this, a recent study has also provided corroborative evidence that suggests Madagascar cyclonic eddies have the potential to be important vectors of connectivity between Madagascar and KwaZulu-Natal, east coast of South Africa (Halo, Penven, et al., 2014). These results demand a better knowledge of the time-evolving capacity of Madagascar eddies to trap waters at their interior as they might contribute significantly not only to the heat and salt budgets of the Agulhas Current system but also to its marine ecosystems, carrying ocean properties which are representative of the Madagascar region.

Traditionally, Lagrangian studies of coherent vortices in the ocean are based on eddy properties derived from surface drifters and/or altimetry-derived products (Beron-Vera et al., 2013; Haller & Beron-Vera, 2013; Lewis et al., 1989; Pérez, 2003; Sangrà et al., 2005), occasionally complemented with full water-column depth measurements undertaken specifically for a given time of their trajectories (Casanova-Masjoan et al., 2017; de Ruijter et al., 2004; Law et al., 2001; Sangrà et al., 2007; Van et al., 2003). In this regard, the global network of Argo floats following a standard configuration can hardly assist, since having parking depths at 1,000 m

depth, floats are unlikely trapped over time within mesoscale eddies. This prevents a robust description of their generation and dissipation phases through the water column. The exception occurs when the core of mesoscale eddies reaches the Argo parking depths and the floats can remain trapped in the eddies (Pegliasco et al., 2015). Accordingly, the recent use of Argo floats following non-standard mission parameters allows higher-resolution research and has proven successful in a handful of recent works (Inoue et al., 2016, 2016; Kouketsu et al., 2016; Riser et al., 2016). Zhang, Li, et al. (2015) used Argo floats with a high sampling frequency to investigate anticyclonic subthermocline eddies related to the subduction of subtropical mode water in the northwest Pacific Ocean. The floats were set on a daily profiling frequency and a park depth of 500 m, profiling from 1,000 m to the surface. Results revealed novel characteristics of subthermocline eddies supporting the potential of Argo floats to track and monitor eddies, particularly if on short repeating cycles. On a similar profiling strategy, the ACE-INBOX project (Inoue, Honda, et al., 2016) deployed 16 profiling floats from June 2012 to July 2013 within a warm-core anticyclonic eddy and used the data to investigate the salinity minimum and its formation process in the Kuroshio-Oyashio mixed water region.

In this work we investigate the 3-D Lagrangian evolution of two Madagascar cyclonic eddies to improve our understanding of the cyclonic eddy contribution of volume, heat, and salt transport from south of Madagascar to the Agulhas Current. To this aim, we designed two surveys to deploy a series of Argo floats in the center of two nonconcomitant cyclonic eddies using ad hoc Argo floats. The surveys were undertaken in April and July 2013, respectively, and non-standard mission parameters were set up to test the trapping of floats by the cyclonic eddies as a function of their park depths and time-resolution profiling against the eddy core depth, nonlinearity, and radius. We combine these in situ hydrographic measurements from the Argo floats with satellite altimeter data and the output of a quasi eddy-resolving ( $1/4^\circ$ ) ocean general circulation model. These diverse, but complimentary, data sources allow us to describe how two Madagascar cyclonic eddies evolve over time from southwest Madagascar toward the African coastline carrying heat and salt anomalies which impact the Agulhas Current.

Recent studies based on data collected from one of the surveys described (July eddy) have already proven the advantages of the experimental design with ad hoc Argo floats (Barlow et al., 2017; Noyon et al., 2018). Barlow et al. (2017) presented a multidisciplinary survey of the cyclonic eddy shed off southwest Madagascar in July 2013. The authors investigated the capacity of Madagascar cyclonic eddies to transport biological material to the South African coast and suggested that increased chlorophyll advected from the SEMC was entrained into the eddy. This was further explored by Noyon et al. (2018), who link enhanced mesozooplankton composition of the Madagascar shelf to the western edge of the eddy, potentially using the strong geostrophic flow south of the eddy as a conduit.

To the best of our knowledge, our analyses represent the first attempt in examining the spatio-temporal changes experienced in full depth by mesoscale eddies (specifically cyclonic) from their generation site toward a western boundary current. The paper is organized as follows. Section 2 details the data and methods. Section 3 presents the results and discussion in subsections which address consecutively the near-surface eddy properties, eddy vertical structure, retention capacity, and associated volume, heat, and salt fluxes of the two Madagascar cyclonic eddies of the study. The main findings and conclusions are summarized in section 4, along with a synopsis on how to set up Argo floats for future mesoscale eddy experiments.

## 2. Data and Methods

Eight Argo floats were deployed in 2013 within the cores of two nonconcomitant Madagascar cyclonic eddies as part of two experiments which aim to study eddy dynamics based on a combination of ad hoc Argo profiling, altimetry, and model data. We name these experiments (and eddies) as the April and July experiments (eddies) following the month in which the floats were deployed. A detailed description of data and methods follows.

### 2.1. Argo-Based Observations

Five Argo floats were deployed on 12 April 2013 crossing a Madagascar cyclonic eddy along an east-west-oriented transect, from its westernmost flank toward its center (Figure 2a). The five SOLO II floats (WMO 1676, 1677, 1678, 1679, and 1680), provided by Woods Hole Oceanographic Institution, were set up to perform daily profiling from 1,000 m to the surface with an initial park depth of 300 m and were equipped with Iridium transmitters. This allowed for two-way communication, and thus, changes to the profiling

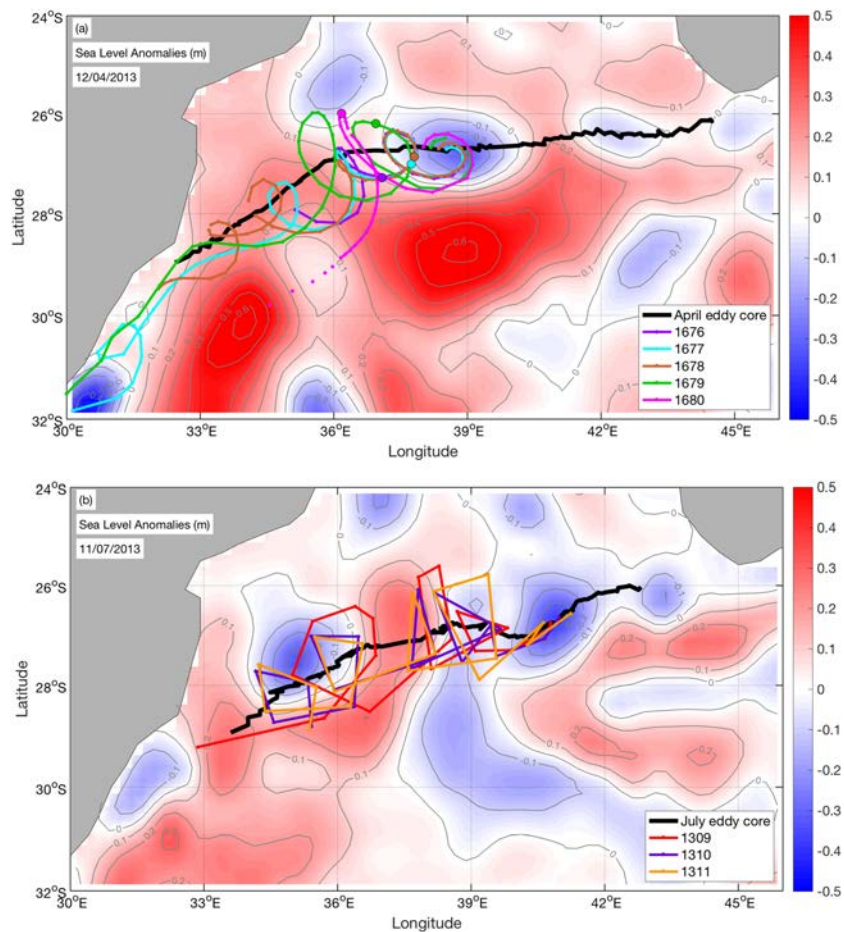


**Figure 2.** Maps of sea level anomaly (m) for the date of the Argo float deployments during the (a) April and (b) July experiments. Dates of deployments are 12 April and 11 July 2013, respectively. Float tracks for each panel end on the date the eddy was last detected in altimetry data: (a) 16 June and (b) 16 October. Positive (negative) sea level anomaly represented by red (blue) shaded contours is indicative of anticyclonic (cyclonic) geostrophic circulation. The thick black lines represent the altimeter-detected eddy core trajectories from the eddy-tracking scheme (Halo, Penven, et al., 2014). Float trajectories are overlaid with colored lines (see legend for Argo float coding). Note the different time resolution of Argo profiling: daily for the April experiment and 5-daily for the July experiment. During the April experiment, park depths were changed after the seventeenth profile (29 April 2013) from 300 m after as follows: Floats 1676 and 1679 remained at 300 m, Float 1677 was changed to 500 m and Float 1678 to 650 m, and Float 1680 was changed to 1,000 m. The seventeenth profile is highlighted with a larger circle over the float trajectories. The park depth during the July experiment remained constant at 500 m. Float parameters are summarized in Table 1.

mission could be made after they were deployed. The floats were ballasted for the Indian Ocean with an additional lithium battery pack to compensate for the above float setup. Modifications of the park depths (listed in Table 1) were performed to evaluate the retention capability of the cyclonic eddy throughout the water column.

Three Apex floats were deployed on 11 July 2013 within a Madagascar cyclonic eddy along a southwest-northeast transect crossing the eddy core (Figure 2b). The three profilers (WMO 1309, 1310, and 1311), provided by the U.K. MetOffice, were set up to perform five-daily profiling from 1,000 m to the surface with a park depth of 500 m to ensure battery life and data collection to the Argo data system. Floats were fitted in this experiment with Argos transmitters (i.e., two-way communication was not possible). Deployment of these floats took place, while a multidisciplinary survey of the cyclonic eddy was completed (Barlow et al., 2017; Noyon et al., 2018).

Mission parameters for each experiment are summarized in Table 1. All Argo data were collected and made freely available by the International Argo Program and the national programs that contribute to it

**Table 1**  
*Setup Parameters of Argo Floats for the April and July Experiments*

Mission parameter	April exp.	July exp.
No. of floats	5	3
Communication	Iridium (2-way)	Argos (1-way)
Profiling frequency	Daily	5-daily
Profiling depth (m)	1,000	1,000
Initial park depth (m)	300	500
Park depth after seventeenth profile: Float code (depth, m)	1676 (300) 1677 (500) 1678 (650) 1679 (300) 1680 (1,000)	1309 (500) 1310 (500) 1311 (500)

(<http://www.argo.ucsd.edu> and <http://argo.jcommops.org>; Argo, 2000). The Argo program is part of the Global Ocean Observing System.

## 2.2. Altimeter Data

We used the Absolute Dynamic Topography (ADT) daily products produced by SSALTO/Duacs and distributed by Copernicus (<http://www.copernicus.eu/>). These gridded altimetry products are computed using multimission data and are the same product as was previously distributed by AVISO+. The new version of SSALTO/Duacs product uses a 20-year reference period (1993–2010) of the sea level anomalies (SLA) with a 1/4° Cartesian grid resolution and projection for the global product (Duacs/AVISO, 2014). The ADT products are calculated using a new Mean Dynamic Topography, which uses the most recent geoid mean field (GOCE DIR-R4) and in situ data set, with an improved processing method (Duacs/AVISO, 2014).

Surface absolute (anomaly) geostrophic velocities derived from the altimetry data are based on the assumption of a geostrophic balance, that is, a balance between Coriolis force and pressure gradient force. Accordingly, altimeter-derived absolute (anomaly) velocities are computed from maps of ADT (SLA) following the geostrophic relationship:

$$u = -g \frac{\partial h}{f \partial y}, \quad v = g \frac{\partial h}{f \partial x}, \quad (1)$$

where  $x$  and  $y$  are the eastward and northward spatial coordinates, respectively;  $u$  is the zonal velocity (positive in the eastward direction);  $v$  is the meridional velocity (positive in the northward direction);  $h$  is the ADT (SLA); and  $g$  is the gravitational acceleration ( $9.8 \text{ m s}^{-2}$ ).

## 2.3. Numerical Model Output: GLORYS2V4

We use the GLORYS2V4 model to complement in situ and remotely sensed measurements and extend the analyses toward a 3-D view of the thermohaline and horizontal velocity structure of the eddies. GLORYS2V4 is performed using the NEMOv3.1 ocean model in the ORCA025\_LIM (1/4° resolution) configuration and is forced by ERA-Interim atmospheric variables. The model has 75 vertical levels and spans over the period 1993–2015. A multidata and multivariate reduced-order Kalman filter technique, based on the Singular Extended Evolutive Kalman filter formulation, is applied to the assimilation of ocean observations to the ocean model. Ocean observations used for the assimilation include delayed-time along-track satellite SLA, daily Reynolds 1/4° Advanced Very-High-Resolution Radiometer (AVHRR)-only sea surface temperature satellite data, and in situ temperature and salinity profiles extracted from the Coriolis Ocean database for ReAnalysis 4 database. These are obtained from all available types of profiling instruments, such as Argo floats; Conductivity, Temperature, and Depth profiles; and Expendable Bathythermography profiles and drifters, in both the surface and subsurface (Cabanes et al., 2013). This reanalysis product (hereafter referred to as the model) is available for download from Copernicus (<http://marine.copernicus.eu>).

The first baroclinic Rossby radius of deformation for the southern Mozambique Channel ranges from 40 km in the south to 60 km in the north (Chelton et al., 1998; Halo, Penven, et al., 2014), while eddies with radii beyond the first baroclinic Rossby radius of deformation have been regularly observed in this region from both in situ and satellite altimetry data (de Ruijter et al., 2004; Nauw et al., 2008; Ponsoni et al., 2016; Quartly & Srokosz, 2004). This supports the suitability of the model resolution to resolve the mesoscale variability in the region south of Madagascar. Furthermore, a number of studies have already shown the value of this

model in capturing the mesoscale dynamics of the Southwest Madagascar Coastal Current (Ramanantsoa et al., 2018; Ramanantsoa et al., 2018) and the South Indian Ocean Countercurrent (Menezes et al., 2016).

#### 2.4. Eddy Identification and Tracking Scheme

We use the eddy detection and tracking scheme developed by Penven et al. (2005) and modified by Halo, Backeberg, et al. (2014). The algorithm is based on both the closed contour (i.e., geometric criteria) and Okubo-Weiss methods of eddy detection. The closed contour method (Chelton et al., 2011) identifies mesoscale eddies as closed loops of sea surface height, given an eddy-length scale small enough to exclude gyres. The Okubo-Weiss method (Okubo, 1970; Weiss, 1991) finds regions in the ocean where the mesoscale vorticity dominates the strain (i.e., the Okubo-Weiss parameter  $[W]$  is negative).

Results in Halo, Penven, et al. (2014) suggest a hybrid eddy detection and tracking scheme is more robust at detecting eddies when compared to using only one of the methods independently of the other. Our cyclonic eddies of study were tracked with reference to their cores and have specified thresholds to ensure minimal subjectivity of their identification. These thresholds include a 2-cm interval between closed contours, a maximum closed loop of 600 km to avoid gyre-sized anomalies, and the number of passes of the Hanning filter equal to two (Halo, Penven, et al., 2014). These three parameters were also shown not to have a highly sensitive effect on the number of eddies detected, which proved the hybrid method to be the most suitable for eddy detection in the southern Mozambique Channel region (Halo, Backeberg, et al., 2014).

### 3. Results and Discussion

#### 3.1. Near-Surface Eddy Properties

In this section we discuss the time evolution and statistics of the April and July eddy properties derived from the SLA altimetry data. First, we provide an overview of mean eddy properties exhibited along the pathway from southwest Madagascar toward the western boundary current (section 3.1.1); second, we describe the Lagrangian evolution of eddy properties (section 3.1.2).

##### 3.1.1. The Pathway From Southwest Madagascar to Southeast Africa

The April and July eddies propagated westward, with a slight poleward deflection, from southwest Madagascar ( $\sim 26^\circ\text{S}$ ,  $43\text{--}44^\circ\text{E}$ ), where the SEMC separates from the continental shelf. The altimeter-derived track of each eddy core is shown in Figure 2 as a black solid line. Both eddies interacted with the Agulhas Current at the KwaZulu-Natal Bight ( $\sim 29^\circ\text{S}$ ,  $32\text{--}34^\circ\text{E}$ ), separately in time, after a travel of 130–137 days ( $\sim 5$  months) at an average propagation speed of  $13\text{--}15\text{ cm s}^{-1}$  (Figure 2).

The mean propagation speed of the April and July eddies was about 2 times the phase speed of nondispersive baroclinic Rossby waves for the range of latitude of Madagascar eddies ( $5\text{--}6\text{ cm s}^{-1}$  at  $25\text{--}30^\circ\text{S}$ ), thus exceeding the prediction from theories for nonlinear vortices (Chelton et al., 2011; Cushman-Roisin, 1994; McWilliams & Flierl, 1979). We attribute the observed high propagation speeds of the April and July eddies being advected in the southern Mozambique Channel to the consistent background currents present in this region. Nevertheless, this mean propagation speed was still much less than the mean rotational speed of both eddies ( $57\text{ cm s}^{-1}$  for the April eddy and  $69\text{ cm s}^{-1}$  for the July eddy). This is important as the ratio of the rotational speed,  $U$ , to the propagation speed,  $c$ , provides a measure of nonlinearity, indicating that both eddies of study were strongly nonlinear (i.e., the nonlinearity ratio exceeds 1). This aspect will be further examined in section 3.3, where we compute the ratio of nonlinearity through the entire water column to determine the trapping depths (and associated volume, heat, and salt fluxes) of each eddy evolving in time and space.

The propagation speeds and directions described above agree well with previous works on Madagascar eddy census. A study based on altimeter data for the period April 1995 to December 2000 found that Madagascar eddies propagate generally in westward and southwestward directions at speeds between  $5$  and  $10\text{ cm s}^{-1}$  (de Ruijter et al., 2004). The sizes of the cyclones and anticyclones were roughly equal when paired, ranging between  $50$  and  $200\text{ km}$  over their lifespan and the amplitudes of their anomalies about  $31\text{--}35\text{ cm}$ . The mean radii of our eddies of study fell within these ranges although with smaller amplitudes: the April (July) eddy with a mean radius and amplitude of  $65\text{ km}$  ( $89\text{ km}$ ) and  $16\text{ cm}$  ( $27\text{ cm}$ ), respectively.

Halo, Penven, et al. (2014) investigated eddy dynamics south of Madagascar using 17 years of altimetry data (1992–2010) and output from the South-West Indian Ocean Model configuration of the Regional Ocean

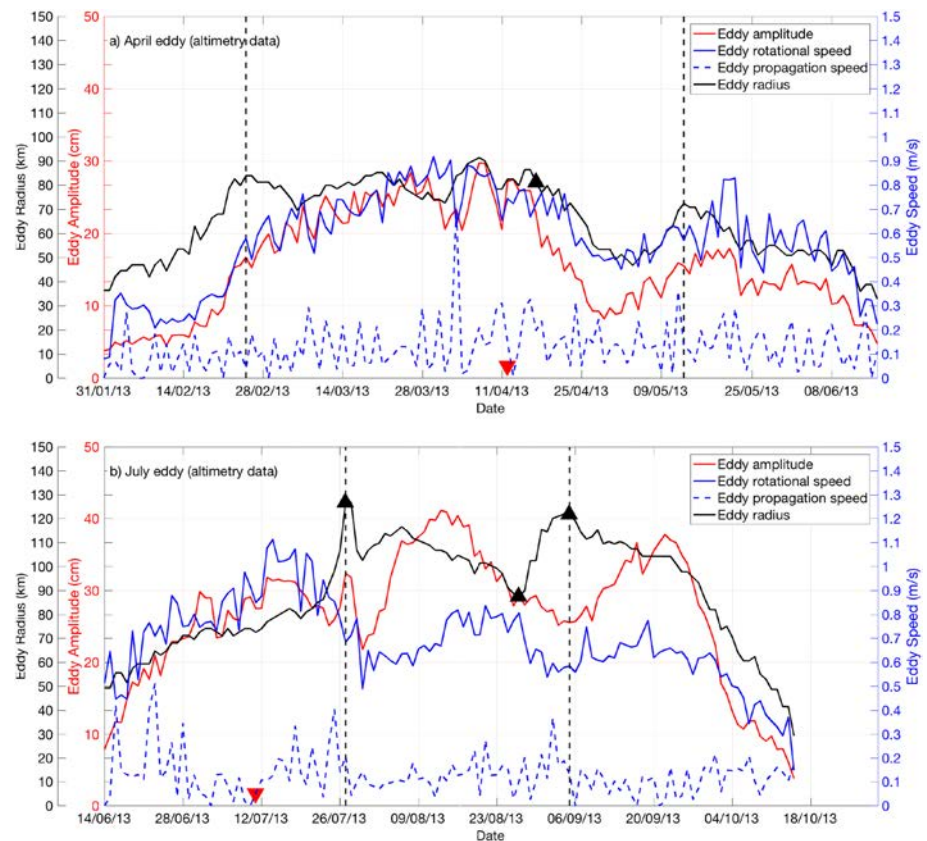


**Figure 3.** Lagrangian evolution of altimeter-derived eddy radius (km, black line), eddy amplitude (cm, red line), eddy rotational speed ( $\text{m s}^{-1}$ , blue line), and daily eddy propagation speed ( $\text{m s}^{-1}$ , blue dashed line) for the (a) April eddy and (b) July eddy as estimated from applying the eddy tracking scheme (Halo, Penven, et al., 2014) over SLA fields. Note that the eddy amplitude is shown in absolute values although cyclonic eddies are identified as a low in the topography field, that is, negative SLA. The black dashed vertical lines indicate the end and start of the eddy growth and decay phases, respectively (the mature stage evolves between both lines). The red inverted triangles indicate the date when Argo floats were deployed. Black triangle symbols along the radius indicate the start date of the cyclonic eddy merging with adjacent cyclonic anomalies, described further in the text.

Modeling System. The authors found that Madagascar cyclonic eddies were the most abundant and longest lived (approximately 4 months) when compared to Madagascar anticyclones. Accounting that only a 10% of the global eddy population are long-lived structures with lifetimes  $>4$  months (Chelton et al., 2011), Madagascar cyclonic eddies stand out as suitable candidates to evolve in time through the growth, mature, and decaying phases before dissipation against the western boundary current system.

### 3.1.2. Lagrangian Evolution

We analyze the Lagrangian evolution of altimeter-derived eddy parameters (radius, amplitude, rotational, and daily propagation speed) for the April and July eddies as presented in Figure 3 from application of the eddy identification and tracking scheme. For simplicity, we plot the eddy amplitude in absolute value, but recall here that cyclonic eddies were identified as a low in the topography field, that is, negative SLA. A summary of eddy characteristics is presented in Table 2, along with values similarly derived from the model data; the comparison between both data sources will be addressed in section 3.3 to support the use of the model for further analyses. Furthermore, we illustrate the key events of the life cycle of each eddy in Figure 4, where a sequence of altimeter-derived absolute geostrophic velocity maps follow the evolution of the April Eddy (panels a–d) and the July Eddy (panels e–h) on selected dates. These dates respond to days over which the April and July eddies interacted with other mesoscale features (labeled on each panel) or against the western boundary.

Generally, the life cycle of an oceanic mesoscale eddy may be summarized as follows. The eddy evolves along its growth phase from a relatively small initial size toward a mature stage, when the eddy growth slows down and its radius remains nearly stable over time. The mature stage ends when the eddy starts to decrease and

**Table 2**

*Eddy Characteristics of the April and July Eddies as Derived From Applying the Automated Eddy Identification and Tracking Scheme Through the Satellite Altimetry and Model Data*

	April E. (S)	April E. (M)	July E. (S)	July E. (M)
Generation at SW Madagascar	26.12° S 44.49° E	26.26° S 43.46° E	26.03° S 42.82° E	26.24° S 42.90° E
Dissipation at KwaZulu-Natal Bight	28.96° S 32.43° E	27.98° S 33.91° E	28.93° S 33.60° E	29.38° S 32.80° E
Lifespan dd/mm (days)	31 Jan. to 16 June (137)	21 Feb. to 02 June (101)	14 June to 16 Oct. (123)	02 June to 30 Oct. (130)
Radius (km)	65.43 ± 15.05	74.53 ± 10.28	88.67 ± 22.39	78.66 ± 15.84
Amplitude (cm)	15.81 ± 7.11	13.44 ± 6.33	26.77 ± 8.71	22.12 ± 7.90
Prop. speed (cm s <sup>-1</sup> )	12.8 ± 9.78	13.7 ± 8.3	14.6 ± 15.01	13.0 ± 8.93
Rot. speed (cm s <sup>-1</sup> )	57 ± 19	42 ± 19	69 ± 17	62 ± 14
Peak radius, (km) (date)	91 (7 April)	89 (23 April)	126 (27 July)	107 (7 Sept.)
Peak ampl., (cm) (date)	30 (7 April)	26 (8 March)	41 (13 Aug.)	34 (2 Aug.)
Peak rot. speed, cm s <sup>-1</sup> (date)	92 (30 March)	87 (7 March)	111 (14 July)	102 (30 July)
Eddy interact.	1 CE	1 CE	3 CEs	3 CEs

*Note.* “S” stands for satellite altimetry data, “M” stands for model data, and “CE” stands for cyclonic eddy. Statistics of a given parameter are presented as the mean ± standard deviation. The number and nature of eddy interactions with other mesoscale features are noted after visual inspection of the full time series of surface horizontal maps from altimetry data.

approach its initial size along the so-called decay phase (Samelson et al., 2014; Zhang, Xue, et al., 2015). In Figure 3, we use black dashed vertical lines to indicate the end and start of the eddy growth and decay phases based on the first and last peaks of the eddy radius, as suggested in Zhang, Xue, et al. (2015). At arrival to the western boundary, both eddies had evolved through well-delimited growth, mature, and decay stages.

The April eddy was first detected on 31 January at 26.12° S, 44.49° E, with an initial radius and amplitude of 36 km and 4 cm, respectively; while the July eddy was first detected on 14 June at 26.03° S, 42.82° E with a larger initial radius of 49 km and similar amplitude about 5 cm (Figure 3). Interestingly, the April eddy evolved toward a mature stage faster than the July eddy; the growth phase lasted for 26 days for the April eddy and 42 days for the July eddy. This might be a response to the time the July eddy, of a larger initial size, required to evolve and reach its peak dimensions.

Through the mature and decay stages, we observed some general similarities (Figure 3). The April eddy collided against the KwaZulu-Natal Bight on 16 June after a total travel of 137 days. As a mature feature (76 days), it propagated with peak dimensions of about 91-km and 30-cm amplitude, decreasing and approaching its initial size of 33-km and 8-cm amplitude along the decay phase (34 days). Roughly, the July eddy experienced an analogous path and arrived at the KwaZulu-Natal Bight on 16 October after a total travel of 123 days. As a mature eddy (39 days), it propagated as a larger feature than the April eddy, having a peak size of about 126-km and 41-cm amplitude. However, the July eddy also decreased its size approaching its initial dimensions along the decay phase (55 days), with a final size of 30-km and 4-cm amplitude.

On closer inspection, we note each eddy-resembled varying structures given the occasional fluctuations of the eddy radius in response to interactions with other mesoscale features. We take the eddy radius as reference of the eddy evolution and compare its trend against the amplitude and rotational speed curves in Figure 3. This allows us to better account for eddy interactions and merger events, highlighting the complexity of studying Lagrangian properties in dynamically active areas. To ease the interpretation, we reference the relationship between eddy radius, amplitude, and rotational speeds. The eddy amplitude relates to rotational speeds following equation (1). A prominent low in SLA is suggestive of a strong cyclonic geostrophic circulation, while the opposite occurs with a prominent high, pointing to a strong anticyclonic circulation. The stronger the spatial gradient of SLA becomes in equation (1), the stronger the rotational speeds of the eddies are. According to this, one finds strengthening of eddy rotational speeds when, for a given eddy radius, the associated low (or high) in SLA intensifies; analogously, eddy rotational speeds slow down when the low (or high) in SLA weakens. The same applies to lows and highs in ADT and the associated absolute geostrophic velocity field.

In principle, the relationship between the eddy radius, amplitude, and rotational speed holds tight in parallel, while the eddy propagates without complex interactions with other mesoscales features and/or physical

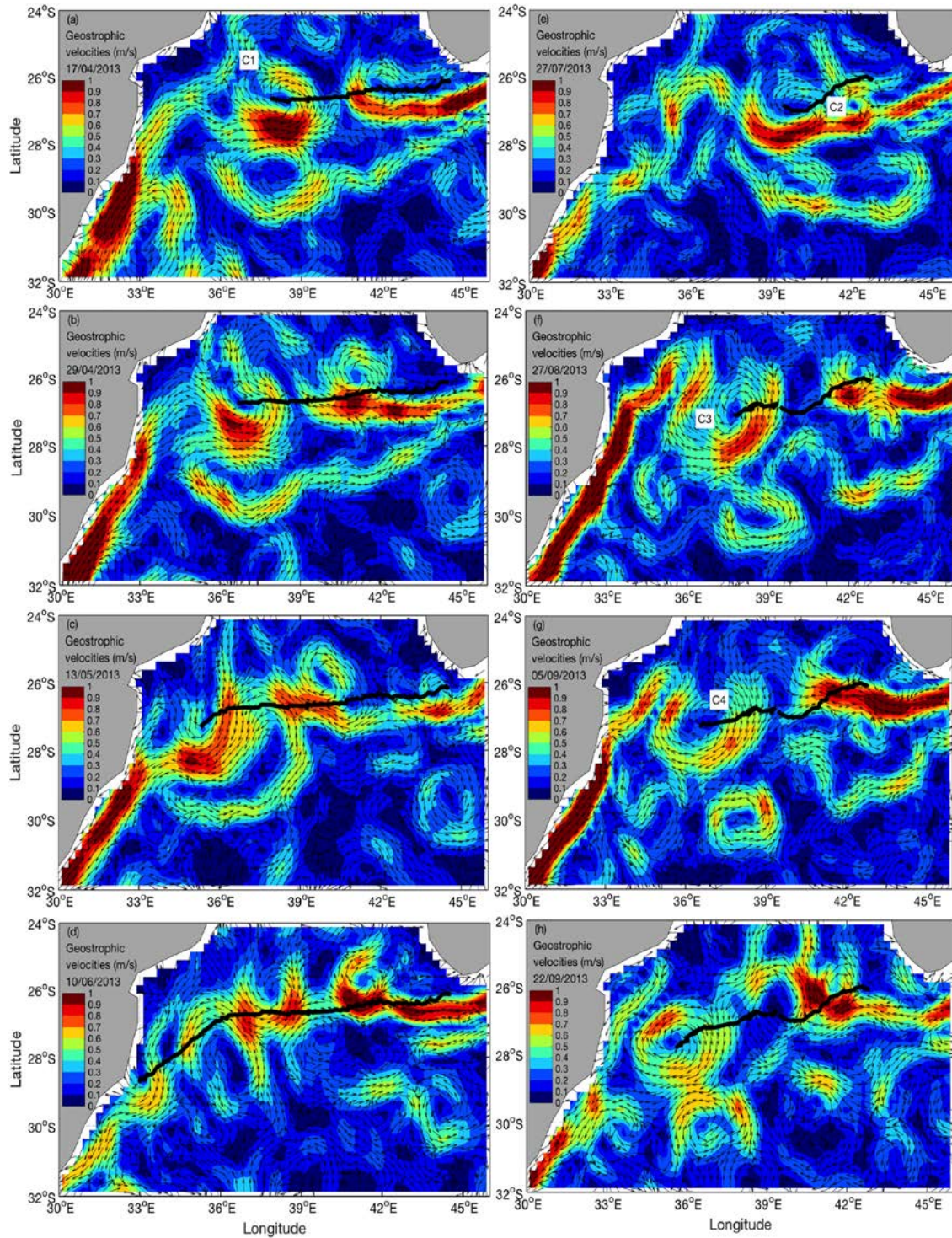


**Figure 4.** Evolution of the April (a–d) and July (e–h) eddies as seen from a set of altimeter-derived geostrophic velocity maps at selected dates. Shades of colors are speed in units of centimeters per second. Arrows represent unit vectors parallel to the vector velocity field. The selected dates refer to key events discussed in the text: (a) 17 April, (b) 29 April, (c) 13 May, (d) 10 June, (e) 27 July, (f) 27 August, (g) 05 September, and (h) 22 September. The eddy core trajectories are shown as thick black lines. Labels with white background overlying the velocity field, and noted as C1–C4, stand for numbered cyclonic features interacting with the April and July eddies.

boundaries. This is the case of the April eddy, whose evolution of the eddy radius, amplitude, and rotational speed followed each other closely through the growth, mature, and decay phases. Along its lifespan, we only detected one merger to another relatively small cyclonic eddy, which originated in the Mozambique Channel. The date when this interaction started is highlighted in Figure 3a with a black triangle. The interaction with this second cyclonic eddy started on 17 April with the elongation of the feature to the northwest (Figure 4a), showing a more complete merger by 29 April (Figure 4b). During the merger, the April eddy decreased both in size and amplitude, while rotational speeds also weakened (Figure 3a). By 13 May, the merger was complete (Figure 4c), and the April eddy exhibited a moderate strengthening just before starting its decay phase (Figure 3a). This occurred about 1 month prior to collision against the Agulhas Current, when the April eddy represented a smaller, weaker cyclonic eddy entering the KwaZulu-Natal Bight from the north and disappearing from the eddy detection and tracking scheme on 16 June 2013 (Figure 4d).

Differently, the July eddy evolved as a larger mesoscale vortex with parameters exceeding those reached by the April eddy (see Table 2) and the tight relationship between the trends of the radius, amplitude, and rotational speed was only clear during the growth and decay stages (Figure 3b). During the mature stage, three noticeable disruptions occurred matching in time the interaction of the July eddy with other smaller cyclonic features to the north and east of it. The dates when these interactions started are indicated with black triangles in Figure 3b and are tracked through a sequence of maps in Figure 4. Two smaller cyclonic eddies were evident to the east and west on 27 July and 27 August, respectively, which eventually merged with the July eddy (Figures 4e and 4f). Toward the end of the July eddy track, further interactions with cyclonic features to the north were also evident on 5 September (Figure 4g), prior to interaction against the western boundary on 22 September (Figure 4h).

As advanced in the previous section, the mean propagation speed of the April and July eddies suggests both features propagated as strongly nonlinear vortices. This is shown in Figure 3 noting that the propagation speeds of both eddies ranged most of their lifespan at rather weaker values than the rotational speeds (cf. blue dashed and solid lines in panels a and b).

### 3.2. Eddy Retention and Vertical Structure Based on Observations

As explained in section 1, Argo floats in this study followed non-standard configurations aiming to test the capability of capturing eddy dynamics if park depths fall within the eddy vertical extent for trapping waters, thus preventing floats from leaving the eddy along their lifespan.

In this section we evaluate the success of Argo floats on being retained within the eddies as they propagated southwestward across the Mozambique Channel based on Argo float trajectories and altimeter-derived eddy properties (sections 3.2.1 and 3.2.2). Furthermore, we select a number of Argo floats sampling the April and July eddy cores and eddy flanks to investigate the Lagrangian evolution of temperature and salinity properties carried by the eddies over time and space (section 3.2.3). Given that floats do not remain stationary or evenly spaced within the eddies, we complement the observational view presented here with further analyses based on model data in subsequent sections.

#### 3.2.1. Eddy Retention: The April Eddy

The April eddy was surveyed on 12 April with five Argo floats deployed from its western edge toward the core, when the eddy was located roughly in the middle of the southern Mozambique Channel, centered at 26.73° S, 39° E, and loosely paired to an anticyclonic eddy as part of a dipolar structure (Figure 2a; see the color code for floats in legend). Over the deployment date, the eddy was about 71 days old, evolving through its mature phase (see the inverted red triangle in Figure 3a).

While Argo floats during the April experiment were all setup to perform daily profiling from 1,000 m to the surface with an initial park depth of 300 m, the initial distances for float deployments ranged among floats from 70 to 15 km off the eddy core. According to the float trajectories in Figure 2a, we present in Figure 5a the time-varying distance of each float to the altimeter-derived eddy core (see the color code for floats in legend). The inset shows the full lifespan of the eddy radius as per reference to Figure 4.

The most prominent feature during the April experiment was the zigzagging of float distances, suggesting the floats were systematically traveling by subsequent times, first, toward the eddy edge and, then, back toward the eddy core. This pattern was followed by all floats for about 1 month of daily profiling (Figure 5a). We suggest that a secondary circulation within the eddy may be accounting for this phenomenon, driving the convergence of floats toward the eddy core and divergence toward the eddy edges according to the time the

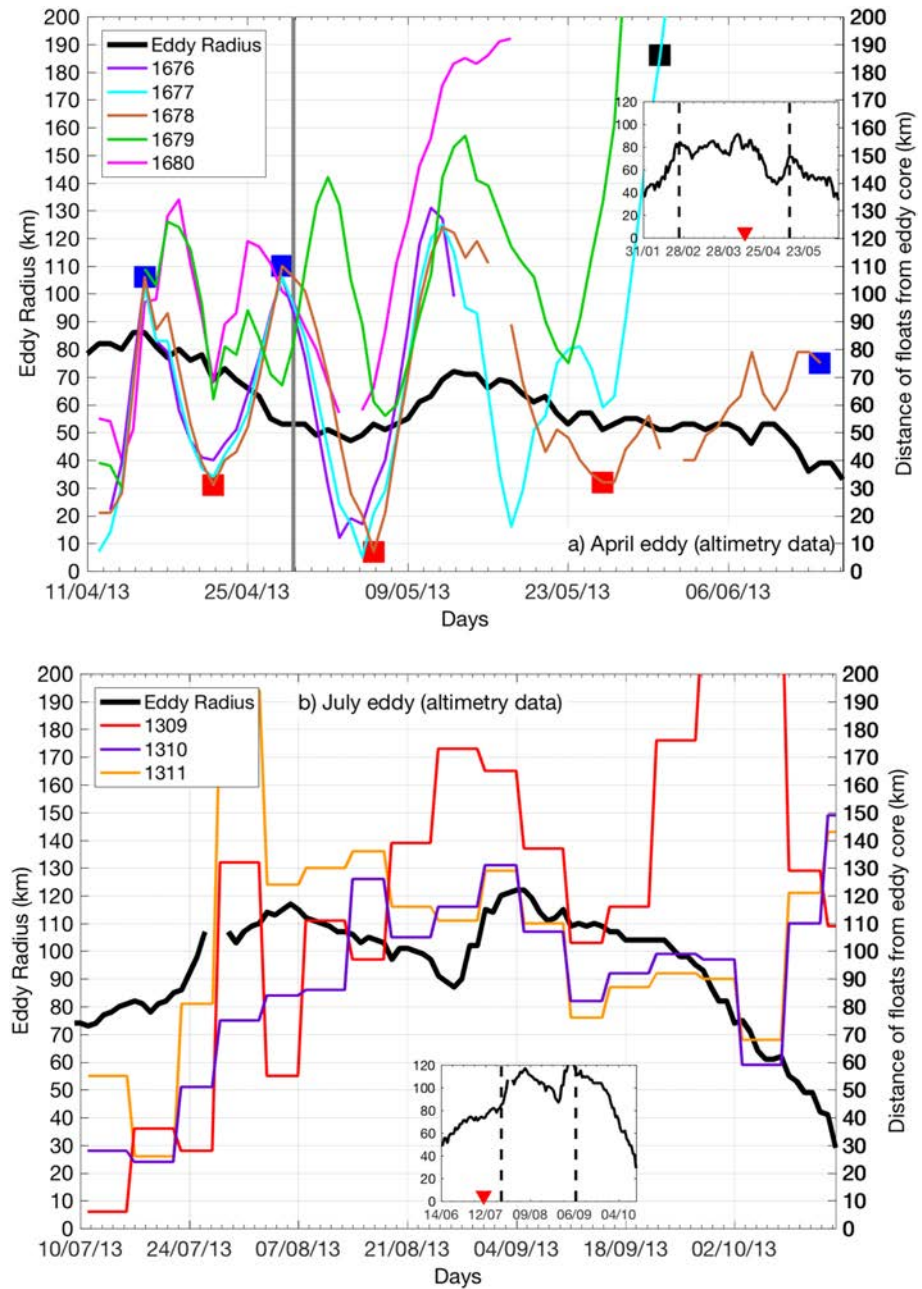


**Figure 5.** Argo float retention within (a) the April eddy and (b) the July eddy as seen from time-evolving distance to the eddy core (see legend for Argo float coding). The time evolution of the eddy radius (thick black line) is shown as indicative of the eddy size. The insets show the full lifespan of the eddy radius evolution, as per Figure 3. Within (a), the blue squares represent the profiles farthest away from the eddy core shown in Figure 6, while red squares show the profiles closest to the eddy core. The black square represents the profile for Float 1677 which enters the Agulhas Current before the eddy, as per Figure 6. The gray solid line in (a) highlights the seventeenth profile where mission parameters were altered.

floats spent drifting both at surface and at the park depths. This pattern also suggests the altimeter-derived eddy radius might be either an underestimation of the actual eddy radius or that the eddy dynamics still have a strong influence in surrounding waters beyond the eddy edges; otherwise, it is hard to account for the systematic convergence of Argo floats back toward the eddy core once they have exceeded the eddy radius in several dozens of kilometers from the eddy core.

At the seventeenth profile (29 April) after deployment during the April experiment, the park depth of the floats was changed from 300 m as follows: Float 1676 and 1679 remained at 300 m (the former stopped communicating after 33 profiles), Float 1677 was changed to 500 m and Float 1678 to 650 m, and Float 1680 was changed to 1,000 m (see a summary of mission parameters in Table 1). We note the merger of the April eddy to another (smaller) cyclonic eddy, as described in section 3.1.2 (Figures 4a–4c), occurred coincidentally to the park depth changes made to the floats. Large colored circles along the float tracks in Figure 2a highlight the float positions where the park depths were modified. In Figure 5a, the seventeenth profile is also indicated (see gray vertical line). As explained in section 1, these changes were configured to assess the effectiveness of Argo floats on capturing eddy dynamics depending on different park depths.

Figure 5a highlights that before the seventeenth profile, all floats were retained by the eddy dynamics, suggesting 300 m as park depth was a suitable choice. One week after the seventeenth profile, the Float 1680 (1,000-m park depth) left the eddy, increasing in time its distance to the eddy core until end of communication. This suggests that 1,000 m as park depth might actually fall out of the range of eddy trapping depths. All other floats (park depths between 300 and 650 m) remained under the influence of the April eddy for at least one extra month (29 April to 23 May); except the Float 1676 (300 m as park depth), which stopped communicating about two weeks after the seventeenth profile while still zigzagging from the eddy edge toward the eddy core.

The Floats 1677 and 1679 (500 and 300 m as park depths) left the April eddy and started their propagation toward the western boundary around 23–27 May, 1 month after the seventeenth profile. This occurred while the floats were circulating around an enlarged merged cyclonic eddy (Figure 4c), likely hampering its return travel toward the eddy core and favoring its exit. These floats reached the western boundary soon afterward and, propagating along the Agulhas Current, increased quickly their distance from the April eddy core (see cyan and green lines in Figures 2a and 5a). Interestingly, the Float 1678 (650 m as park depth) remained within the eddy to the end of its lifespan, upon arrival to the western boundary.

### 3.2.2. Eddy Retention: The July Eddy

The July eddy was surveyed with three Argo floats deployed during the eddy growth phase, when the eddy was 27 days old on 11 July (Figures 2b and 3b). The floats were deployed from southwest to northeast crossing the eddy center and falling within a range of 60 km from the eddy core. All floats were set up to perform five-daily profiling from 1,000 m to the surface with a park depth of 500 m, which was not modified after deployment as it occurred during the April experiment.

Interestingly, the float deployed closest to the eddy core (Float 1309; red line in Figures 2b and 5b) eventually moved the furthest away, while the other two (Floats 1310 and 1311) remained closely associated with the eddy radius to the end of the eddy's lifespan. However, it is worthwhile noting the exit of the Float 1309 occurs after 2 months of the instrument being under the influence of the eddy dynamics, thus further supporting the suitability of 500 m as Argo park depth for the float to be retained within the eddy. Similar to what was observed from the Argo float distances to the April eddy core (Figure 5a), we also observe the Argo float distances to the July eddy core zigzag in space and time around the eddy edges, although the lower time resolution of the Argo profiling during this experiment hampers a clear visualization of the phenomenon.

Results in sections 3.2.1 and 3.2.2, based on Argo float trajectories and altimeter-derived eddy properties, suggest that the most suitable configuration (among tested options) to capture eddy dynamics of Madagascar cyclonic eddies was daily profiling with park depths between 300 and 650 m. On the one hand, the park depth at 1,000 m tested during the April experiment seemed to exceed the vertical extent of the eddy, while shallower park depths resulted in floats drifting over longer periods of time within the eddies. On the other hand, the five-daily profiling of the July experiment appears to miss details of the apparently rapid secondary circulation patterns suggested by the convergence/divergence of the floats toward/from the eddy core and which demand further investigation. In section 3.3, we assess the vertical extent of the April and July eddies as they evolve in time and space based on model data, supporting further the suitability of Argo park depths between 300 and 650 m following estimates of nonlinearity through the water column (a measure of eddy retention) and associated eddy trapping depths.

### 3.2.3. Vertical Structure

To illustrate the evolution of the vertical structure of a prototypical Madagascar cyclonic eddy as seen from Argo profiling, we present in Figure 6 a series of vertical profiles of (a) conservative temperature, (b) absolute salinity, and (c) potential density from Float 1678, which remained with the April eddy the longest at daily

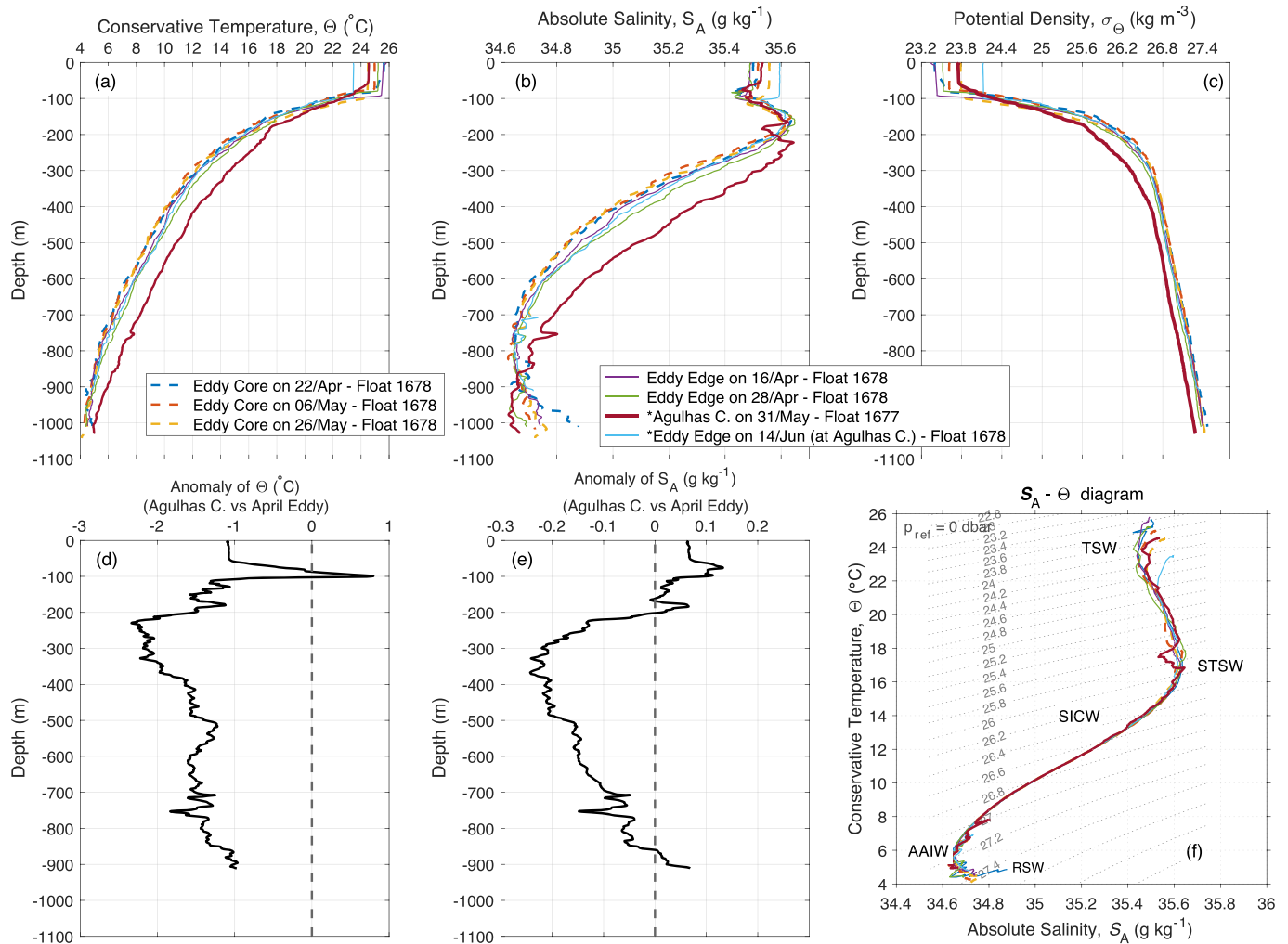


**Figure 6.** Argo-based vertical profiles of (a) conservative temperature, (b) absolute salinity, and (c) potential density ( $\text{kg m}^{-3}$ ) representative of properties along the eddy edge (solid lines) and within the eddy radius (dashed lines) as identified by blue and red squares, respectively, in Figure 5a (see Float 1678, brown line, sampling the April eddy). The anomaly of (d) conservative temperature and (e) absolute salinity was calculated from comparison between a profile from Float 1677 sampling the Agulhas Current and a profile from Float 1678 sampling the cyclonic eddy while interacting with the Agulhas Current at nearly the same location ( $29.5^{\circ}\text{S}$ ,  $32.1\text{--}32.3^{\circ}\text{E}$ ) but 15 days apart. (f) Conservative temperature versus absolute salinity diagram with indication to water masses: Tropical Surface Water (TSW), Subtropical Surface Water (STSW), South Indian Central Water (SICW), Antarctic Intermediate Water (AAIW), and Red Sea Water (RSW).

profiling. We use results in Figure 5a to select the profiles of interest according to its spatial closeness to the eddy core and eddy flanks, so that we can assess, separately, differences in properties carried by the eddies over time and space. The selected profiles falling close to the eddy edges are shown with blue squares in Figure 5a, while profiles close to the altimeter-detected eddy core are shown with red squares. Also in Figure 5a, the black square along the curve for Float 1677 indicates an Argo profile which sampled the Agulhas Current 15 days before Float 1678 sampled nearly the same location ( $29.5^{\circ}\text{S}$ ,  $32.1\text{--}32.3^{\circ}\text{E}$ ) while still retained within the April eddy before it interacted with the Agulhas Current (see legend in Figure 6). The comparison between these two Argo profiles from different floats (1677 and 1678) allows us to estimate the magnitude of temperature and salinity anomalies carried by the April eddy upon interaction with the Agulhas Current (Figures 6d and 6e). Based on all the Argo profiles described above, the variability of water masses is presented following the  $\theta/S_A$  diagram in Figure 6f.

Among the profiles sampled within the April eddy (both the core and flanks), surface waters displayed the highest variability as a consequence of direct and rapid ocean-atmosphere interactions modifying the upper  $\sim 100$  m of the water column, where Tropical Surface Water ( $\sigma_{\theta} < 25.5 \text{ kg m}^{-3}$ ; Beal et al. (2006)) becomes cooler and saltier over time as the eddy propagates southwestward (Figures 6a–6c and 6f). At 150–200 m,

all eddy profiles presented a subsurface salinity maximum approaching 35.65, characteristic for Subtropical Surface Water (Gründlingh et al. (1991)), and below, a rather less variable domain of South Indian Central Water between 300 and 900 m (8–14°C, 34.6–35.4 g kg<sup>-1</sup>; Emery (2001)). Deeper than 900 m, eddy profiles showed a progression from diluted Red Sea Water (RSW) toward Antarctic Intermediate Water (AAIW) signals. The RSW signal, originated further north, opposes to the AAIW signal, originated further south, on that the latter was characterized by salinities lower than 34.6 g kg<sup>-1</sup> while RSW was found commonly saltier than 34.6 g kg<sup>-1</sup>. The progressive decrease in diluted RSW and increase in AAIW as the floats traveled southwestward suggest the eddy capability to retain temperature and salinity properties over time along its pathway to the African coastline might not reach beyond 900 m. Above this depth level and up to 100 m, all eddy profiles followed each other remarkably closely as the eddy evolved in time and over space, especially profiles sampling the eddy core, which was suggestive of the retention capability of ocean properties of the eddy. We note the description of water masses characterizing the April eddy agreed well with that reported in de Ruijter et al. (2004), focused on the first 400 m of the water column, and based on direct measurements of temperature and salinity surveying a Madagascar cyclonic eddy in the middle of the southern Mozambique Channel.

When compared to the Argo profile which sampled the Agulhas Current (dark red lines in Figures 6a–6c and 6f), the eddy profiles exhibited a distinctive cooler and fresher vertical distribution of ocean properties highlighted as negative temperature and salinity anomalies which extended through the water column down to 900 m, except for a relatively shallow and weak positive salinity anomaly within the upper 200 m (Figures 6d and 6e). These negative temperature and salinity anomalies were as large as –2 °C (0–900 m) and –0.2 g kg<sup>-1</sup> (200–900 m), respectively. These results support the potential of Madagascar cyclonic eddies to transport large temperature and salinity anomalies effectively from Madagascar to southeast Africa, from the surface down to about 900 m.

In the next section, we use model data to provide first estimates of the volume, heat, and salt fluxes associated to the April and July eddies down to their time-varying trapping depth as they propagated toward the western boundary, thus evaluating how these fluxes may change in time according to the growth, mature, and decay phases of the eddies.

### 3.3. Vertical Structure, Eddy Retention, and Fluxes Based on Model Data

In this section we complement the observational view in previous sections and extend our analyses supported on model data to examine, first, the time-evolving vertical structure of the April and July eddies through their growth, mature, and decay phases (section 3.3.1), and second, their time-varying retention capacity and associated volume, heat, and freshwater fluxes (section 3.3.2). The aim is to assess the major changes which characterize the Lagrangian evolution of these features upon interaction with the Agulhas Current.

#### 3.3.1. Vertical Structure

Figure 7 shows the Lagrangian evolution of near-surface eddy properties of the April and July eddies calculated using the eddy detection and tracking scheme of Halo, Penven, et al. (2014) over model data. These eddy properties are model eddy radius (black line), amplitude (red line), rotational speed (solid blue line), and the daily eddy propagation speed (dashed blue line) for both the April and July eddies (panels a and b, respectively). We use here the same axis limits (particularly with reference to time) that are used in Figure 3 (altimeter-derived properties) to ease comparison between data sources, for which a summary is also provided in Table 2.

As compared to the altimeter-derived Lagrangian evolutions, we find the model April eddy was detected later in the eddy tracking scheme (21 February), further west (26.26° S, 43.46° E), and disappeared sooner (02 June), slightly north of the KwaZulu-Natal Bight (27.98° S, 33.91° E), lasting 101 days in total (Table 2). Regarding the model July eddy, its detection was slightly later (22 June) in a very similar position as the altimetry July eddy but lasted longer (30 October) and dissipated similarly off of the KwaZulu-Natal Bight. The above differences being noted, the overall comparison of spatial and time scales of the model April and July eddies showed a good agreement with eddy statistics of the altimeter-derived properties in Table 2 and their corresponding Lagrangian evolution in Figure 3. This encourages us to extend our analyses further based on the model data.

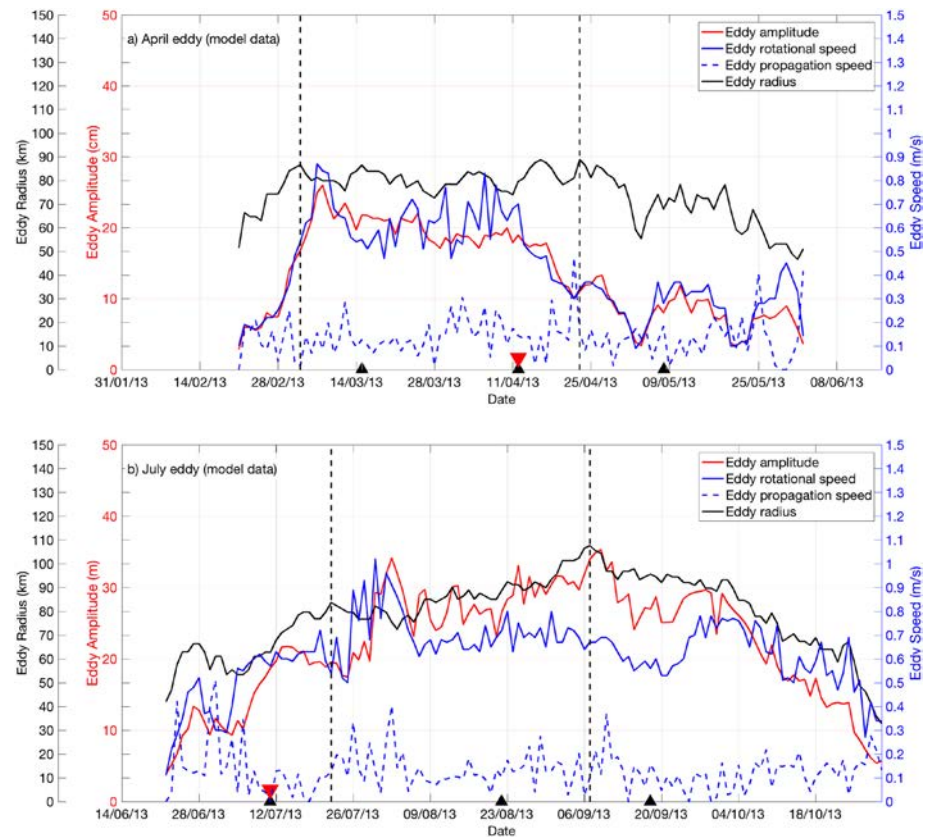


**Figure 7.** Lagrangian evolution of modeled-derived eddy radius (km, black line), eddy amplitude (cm, red line), eddy rotational speed ( $\text{m s}^{-1}$ , blue line), and daily eddy propagation speed ( $\text{m s}^{-1}$ , blue dashed line) for the (a) April eddy and (b) July eddy as estimated from applying the eddy tracking scheme (Halo, Penven, et al., 2014) over model. The red inverted triangles indicate the deployment of floats within the eddies. The black dashed vertical lines indicate the end and start of the eddy growth and decay phases, respectively (the mature stage evolves between both lines). Black triangle symbols indicate the the dates of the nonlinear profiles plotted in Figure 11.

Following the model-derived Lagrangian evolution of the April and July eddies in Figure 7, we present in Figure 8 a set of horizontal maps of surface velocity ( $\text{m s}^{-1}$ ) for selected dates. These dates were representative of the eddy growth, mature, and decay phases of each eddy. We use these maps, first, to describe the eddy evolution at surface and, second, to identify the latitudes over which to extract zonal transects to investigate the time-varying vertical structure of the eddies as they propagate toward the western boundary.

Figures 8a and 8d show at the surface a recently formed Madagascar cyclonic eddy, paired to an anticyclonic eddy as part of a dipolar structure. The dates are 3 March and 11 July, respectively, and captured the April and July eddies during their growth phase. Next, panels b (12 April) and e (22 August) show the eddies while crossing the southern Mozambique Channel during their mature phase, propagating southwestward as well-developed and dynamically strong mesoscale features. Lastly, panels c (8 May) and f (19 September) capture the eddies as decaying features prior to interaction with the Agulhas Current.

On each panel of Figure 8, two black solid lines are overlaid. The zonal lines indicate the location of the zonal transects extracted from the model to illustrate the spatiotemporal evolution of the vertical structure of the April and July eddies (Figures 9 and 10). The meridional lines indicate the intersecting location of the eddy center, shown as a dashed vertical line in Figures 9 and 10 to highlight the position of the April and July eddies, respectively. These vertical sections present the conservative temperature, absolute salinity, potential density, and meridional velocity anomalies along a sequence of zonal cross-channel transects which intersect the April and July eddies as they progressed across the southern Mozambique Channel.

Generally, the April and July eddies exhibited an analogous evolution of the vertical structure with only a few differences. The April eddy presented a subsurface negative anomaly of temperature from 200 m down to 1,100 m during its growth phase, with a relatively shallow positive anomaly from the surface down to

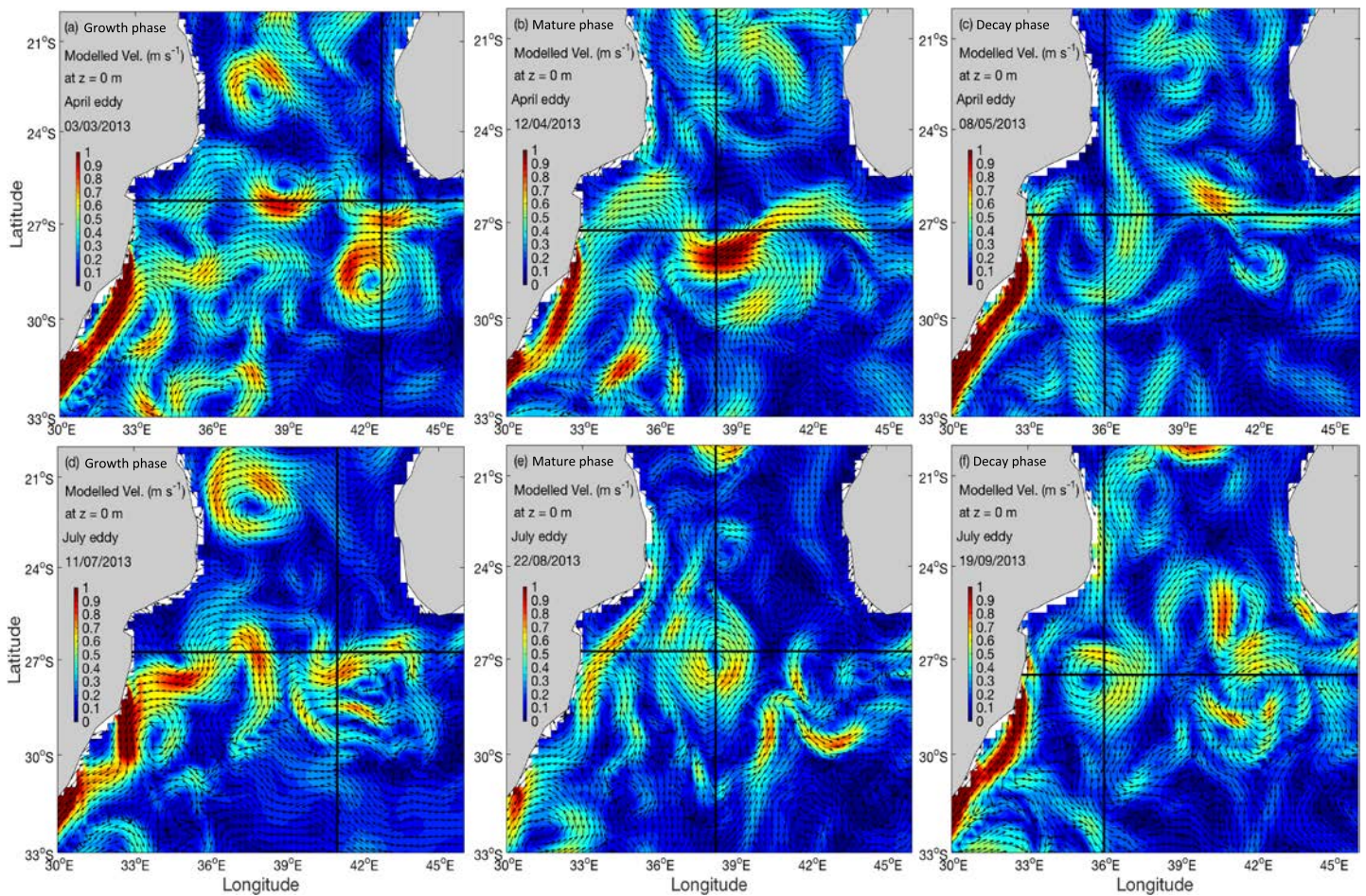


**Figure 8.** Horizontal maps of modeled surface velocity ( $\text{m s}^{-1}$ ) at selected dates which capture the growth, mature, and decay phases of the April eddy. For the April eddy, the selected dates are (a) 3 March, (b) 12 April, and (c) 8 May. For the July eddy, the selected dates are (d) 11 July, (e) 22 August, and (f) 19 September. Overlaid on to the core of the cyclonic eddy of study are the zonal transects selected for each date, as shown in Figures 9 and 10.

200 m (Figure 9a). As the eddy evolved toward a mature stage across the southern Mozambique Channel, the subsurface negative anomaly increased and extended to just below 100 m down to 1,500 m, squeezing the positive anomaly to a lens-like structure (Figure 9b). This structure was maintained upon arrival to the western boundary through the decay phase of the eddy. The subsurface negative anomaly strengthened vertically with the positive lens-like anomaly seemingly joining up with a positive anomaly adjacent to the African coastline (Figure 9c). The vertical structure of the anomaly temperature field for the July eddy followed an analogous evolution to that found for the April eddy, but no lens-like positive anomaly at the surface was apparent (Figures 10a–10c).

A similar structure of subsurface negative anomaly with a positive anomaly above evolving in time was also evident for the salinity field of the April and July eddies (Figures 9d–9f and 10d–10f). The subsurface negative anomaly, which extended from 200 m to about 1,000 m, also strengthened vertically through the growth, mature, and decay phases. According to the above pattern, both eddies carried a vertically elongated positive anomaly of potential density, which strengthens in time. This positive anomaly extended from 150 m down to 1,500 m for the April eddy, with a lens-shaped negative anomaly above (Figures 9g–9i); while the July eddy did not present such a surface negative anomaly (Figures 10g–10i). Remarkably, the vertical sections of meridional anomaly velocities for the April and July eddies showed relatively high and deep-reaching rotational speeds, suggesting these eddies were strongly nonlinear through the water column (Figures 9j–9l and 10). Peak rotational speeds were as high as  $0.4\text{--}0.5 \text{ m s}^{-1}$  and extended down to 700–1,000 m during the mature phase in both eddies and shallower depths of 300–500 m during the growth and decay phases.

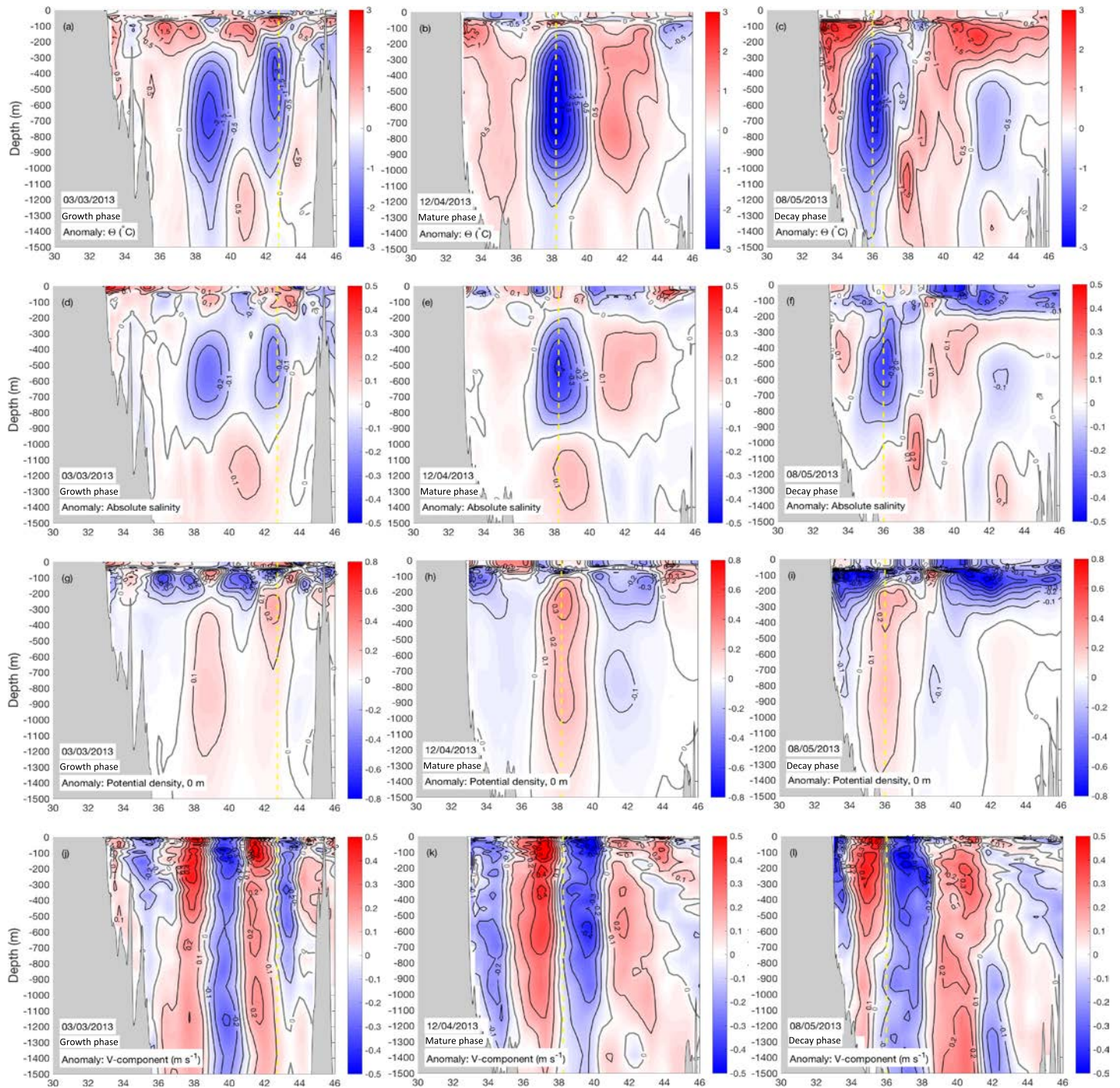


**Figure 9.** Lagrangian evolution of the April eddy as seen from zonal sections crossing the southern Mozambique Channel at different latitudes according to the position of the eddy core at selected dates: 15 March, 12 April and 8 May 2013. These dates capture the eddy growth, mature, and decay phases and highlight the time-evolving anomalies of conservative temperature (a–c), absolute salinity (d–f), potential density (g–i), and meridional velocity (j–l). Positive (negative) shades of colors for velocity denote equatorward (poleward) velocities. See Figure 8 for location of each corresponding zonal transect.

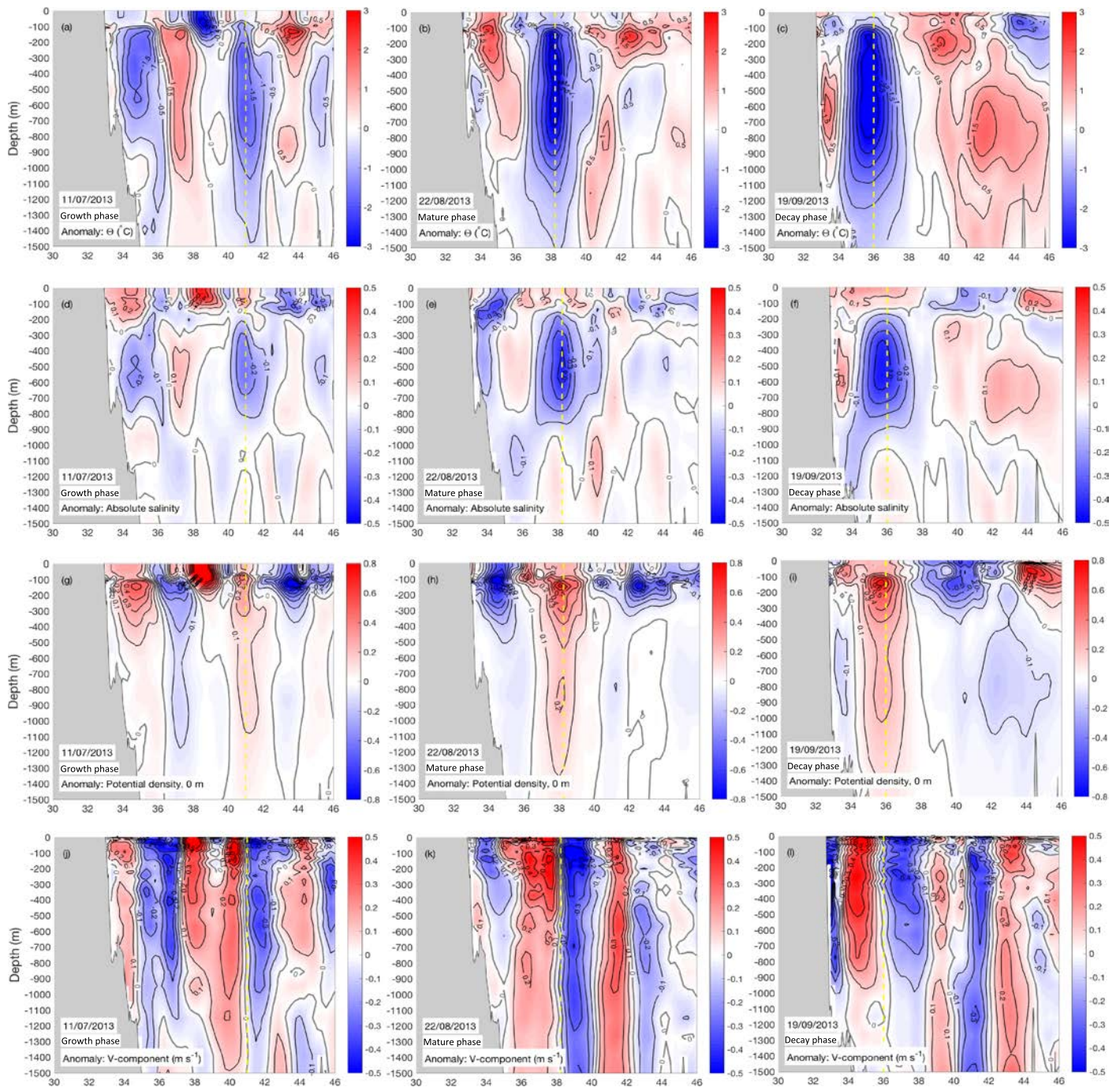


**Figure 10.** Lagrangian evolution of the July eddy as seen from zonal sections crossing the southern Mozambique Channel at different latitudes according to the position of the eddy core at selected dates: 11 July, 22 August, and 18 September 2013. These dates capture the eddy growth, mature, and decay phases and highlight the time-evolving anomalies of conservative temperature (a–c), absolute salinity (d–f), potential density (g–i), and meridional velocity (j–l). Positive (negative) shades of colors for velocity denote equatorward (poleward) velocities. See Figure 8 for location of each corresponding zonal transect.

The dynamic vertical structure of the modeled April and July eddies described so far agrees well both in qualitative and quantitative terms with the eddy vertical structure of rotational speeds presented in de Ruijter et al. (2004), showing deep-reaching strong velocities around  $0.3\text{--}0.4\text{ m s}^{-1}$  down to  $750\text{--}1,000\text{ m}$ . Also, the vertical structure of negative temperature and salinity anomalies in the modeled eddies agreed well with Argo-based anomalies reported in the previous section, although the model data showed slightly higher anomalies than those derived from the Argo profiles with peak anomalies reaching  $-2\text{ }^{\circ}\text{C}$  between  $0$

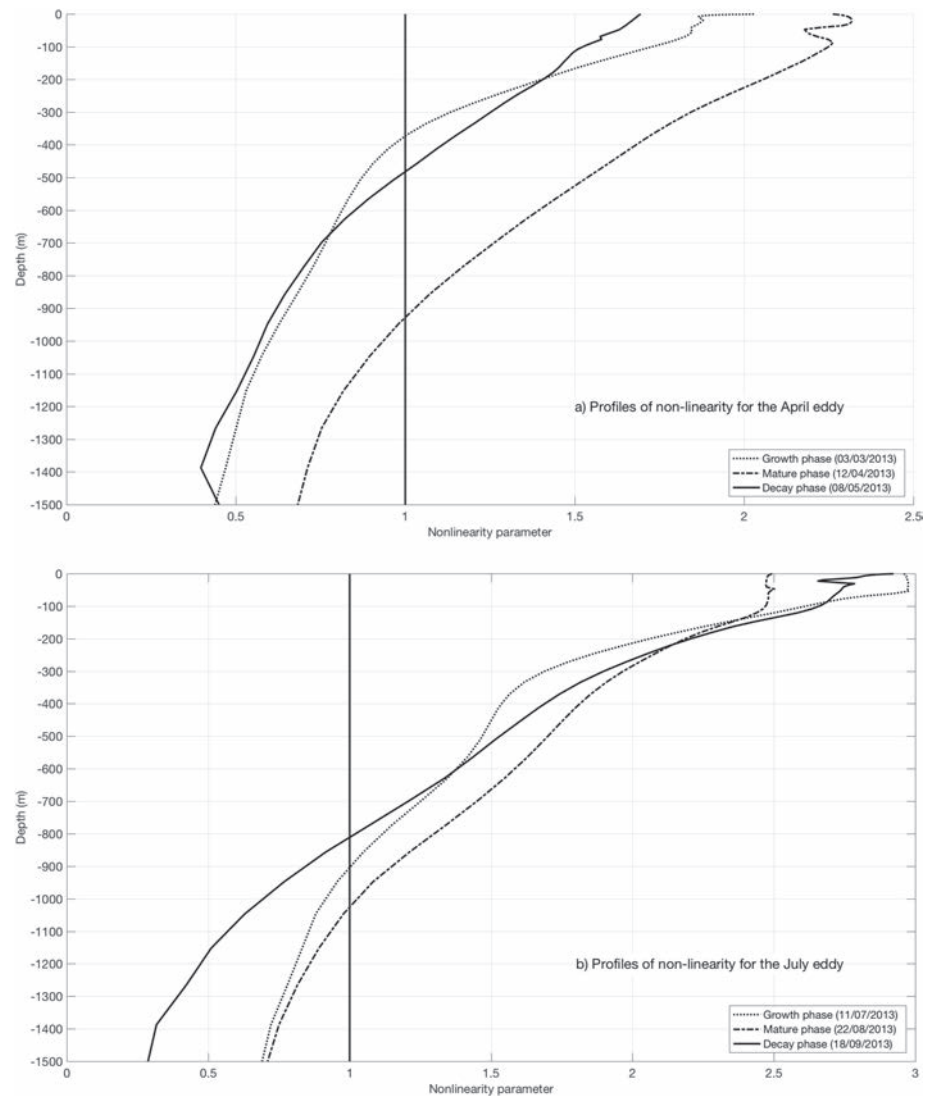


**Figure 11.** Profiles of nonlinearity (unitless) with depth (m) for the growth (blue line), mature (red line), and decay phases (black line) of the (a) April and (b) July eddies as they cross the southern Mozambique Channel (see legend). The black vertical lines indicate a nonlinearity ratio of 1. Depths exceeding this value respond to the vertical extent over which the eddy is capable of transporting water effectively.

and 900 m and  $-0.2 \text{ g kg}^{-1}$  between 200 and 900 m. These results encourage us to examine further the eddy retention capacity and associated fluxes based on model data.

### 3.3.2. Eddy Retention and Associated Volume, Heat, and Freshwater Fluxes

As advanced in section 3.1.1, mesoscale eddies are capable of trapping water within their cores if the ratio between rotational speed,  $U$ , and propagation speed,  $c$ , is greater than one (Chelton et al., 2011; McWilliams & Flierl, 1979; Robinson, 1983). Where this ratio exceeds five, the eddy can then be considered highly nonlinear as per Chelton et al. (2011). This relationship is denoted in Figure 7 by comparing the rotational eddy speed (blue solid line) to the daily propagation speed (blue dashed line). Rotational speed through the water column was extracted from the modeled velocity maps as a vertical profile at the location of maximum speed (Ning et al., 2019) within the eddy contours detected by the eddy identification and tracking scheme. The eddy was considered nonlinear where the eddy rotational speed was above the daily propagation speed, which occurred for the majority of the time for both the April and July model eddies.

Based on the model vertical sections selected in Figures 9 and 10 to capture the growth, mature, and decay phases of the April and July eddies, we present in Figure 11 the time-varying nonlinearity ratio with depth of the April and July eddies through the water column at those same dates. The degree of nonlinearity was

conservatively estimated at each date and eddy by confronting the mean averaged rotational speed at every depth level ( $U$ ) against the mean propagation speed ( $c$ ) estimated over the dates of interest. Also, we assumed the eddies move as bulk entities at all levels taking the propagation speed constant along the vertical. The vertical distributions of the nonlinearity derived in this manner allow us to estimate the depths over which the eddy has retention capability to transport ocean properties along its lifespan.

Notably, both eddies exhibited a similar time-varying evolution of nonlinearity with depth, although the model July eddy presented overall greater trapping depths than the model April eddy, likely as a consequence of its larger size and stronger rotational speeds. Thus, eddy retention increased from initially shallow values to deepest trapping depths as the eddy grew and reached its mature stage, when rotational speeds were stronger and deep reaching. Toward the decay phase of the eddies, trapping depths decreased accordingly. Following this pattern, the model April eddy showed trapping depths from the surface to 373 m during its growth phase, evolving to 928 m during the mature phase and, again, shallower trapping depths about 483 m during the decay phase (Figure 11a). Analogously, the model July eddy presented an increase of trapping depths from 905 m during the growth phase to 1,026 m during the mature phase and 812 m through its decay (Figure 11b).

Previous results suggested Madagascar cyclonic eddies have the ability to advect mass, heat, and freshwater in distinct depth layers, depending on the ratio between their rotational and propagation speeds. We take the estimates of time-varying trapping depths for the model April and July eddies and combine them with the temperature and salinity anomalies shown in Figures 9 and 10 through the growth, mature, and decay phases to calculate the available heat and salt contents (AHA, ASA) following (Barceló-Llull et al., 2017; Dilmahamod et al., 2018):

$$AHA = \int_{z_{\text{trap}}}^0 \int_0^{Rc} \rho_0 C_p \Theta'(2\pi r) dr dz, \quad (2)$$

$$ASA = \int_{z_{\text{trap}}}^0 \int_0^{Rc} \rho_0 S'_A(2\pi r) dr dz, \quad (3)$$

where  $z$  is the vertical coordinate (depth, m),  $z_{\text{trap}}$  is the trapping depth (m),  $\rho_0$  is the mean upper ocean density ( $1,026 \text{ kg m}^{-3}$ ),  $C_p$  is the specific heat capacity ( $4,000 \text{ J}\cdot\text{kg}^{-1} \cdot \text{°C}^{-1}$ ), and  $r$  is the eddy radius (m). Then temperature and salinity anomalies ( $\Theta'$  and  $S'_A$ , respectively) are calculated comparing model daily fields of the selected dates of study against the corresponding multiyear-averaged monthly field over the period 1993–2015.  $\Theta'$  and  $S'_A$  are integrated over the eddy-core area by assuming a circular symmetrical shape and then vertically integrated over the eddy vertical extent for each eddy phase (from the surface down to the trapping depth). We also integrate radially from the eddy center to the eddy-core radius, with  $Rc$  being the eddy radius. A 0.001 factor is used for ASA so as to convert salinity to salinity fraction (kg of salt per kg of seawater). We complete our calculations with estimates of the associated volume, heat, and salt fluxes following (Dilmahamod et al., 2018; Dong et al., 2014):

$$V_e = c \int_{z_{\text{trap}}}^0 2r dz, \quad (4)$$

$$Q_{\text{eh}} = c \int_{z_{\text{trap}}}^0 \rho_0 C_p \Theta'(2r) dz, \quad (5)$$

$$Q_{\text{es}} = c \int_{z_{\text{trap}}}^0 \rho_0 S'_A(2r) dz, \quad (6)$$

where  $V_e$  is eddy-driven volume transport in units of Sverdrups ( $1 \text{ Sv} = 10^6 \text{ m}^3 \text{ s}^{-1}$ ),  $Q_{\text{eh}}$  is eddy-driven heat flux in Watts,  $Q_{\text{es}}$  is eddy-driven salt flux and in kilograms per second, and  $c$  is the mean eddy propagation speed. The vertical integral is computed by discrete summation over interpolated vertical levels.  $c$  is calculated as the mean of 5 days centered around the selected date (e.g., 10–14 April for 12 April). Also, we take  $c$  as a positive so that the sign in fluxes reveals the nature of the temperature and salinity anomalies they transport. Lastly, salt fluxes are discussed in terms of freshwater fluxes (unit: Sv), with  $Q_{\text{fw}} = -Q_{\text{es}}/(\rho_0 S_o)$ , where

**Table 3**

*Vertical Extent, Eddy Radius, Propagation Speed, Volume, Volume Transport, Thermohaline Contents, and Associated Heat/Freshwater Flux of the April and July Eddies Through Their Growth, Mature, and Decay Phases*

Property	Growth phase April eddy 3 March	Mature phase April eddy 12 April	Decay phase April eddy 7 May	Growth phase July eddy 11 July	Mature phase July eddy 22 August08	Decay phase July eddy 18 September
Vertical extent (m)	373	928	483	905	1,026	812
Radius (km)	86.45	79.59	67.83	62.80	88.83	94.46
Propagation speed (m s <sup>-1</sup> )	0.14	0.13	0.18	0.13	0.17	0.11
Volume (10 <sup>12</sup> m <sup>3</sup> )	8.75	18.46	6.98	11.21	25.43	22.76
Volume transport (Sv)	9.02	19.20	11.92	14.54	31.53	17.48
AHA (10 <sup>18</sup> J)	-19.35	-133.85	-23.09	-55.19	-196.32	-203.63
Heat flux (PW)	-0.02	-0.1	-0.04	-0.07	-0.2	-0.2
ASA (10 <sup>10</sup> kg)	-12.80	-321.48	-102.22	-122.58	-404.63	-483.02
Freshwater Flux (Sv)	0.003	0.09	0.04	0.04	0.14	0.10

$S_o = 35$  psu (salt mass fraction) is the mean upper ocean salinity. The resultant property contents and fluxes associated with the April and July eddies are presented in Table 3, where positive (negative) heat fluxes mean eddy-driven warming (cooling) and positive (negative) freshwater fluxes mean eddy-driven freshening (salt contribution).

The mean estimates of cross-sectional volume transport (equation (4)) of the April and July eddies were about  $13.4 \pm 5.2$  and  $21.2 \pm 9.1$  Sv, respectively, taking as reference estimates from the three eddy phases (Table 3). These estimates compared well with the cyclonic eddy observed in de Ruijter et al. (2004), which accounts for a cross-sectional volume transport of about 14.4 Sv from the surface down to 1,000 m given an eddy radius of 120 km and a propagation speed of 6 cm s<sup>-1</sup>. As derived from Lowered-Acoustic Doppler Current Profiler (L-ADCP) observations, these authors reported a larger mean volume transport of about 33 Sv from the flow around the cyclonic eddy, taken from the surface down to 1,000 m. At a rate of four to six dipole structures per year (de Ruijter et al., 2004; Ridderinkhof et al., 2013), one could expect from our estimates for a mean decaying cyclonic eddy between 58.8 and 88.2 Sv reaches the Agulhas Current per year with SEMC waters entrapped (a mean decay eddy transports ~14.7 Sv with reference to values in Table 3).

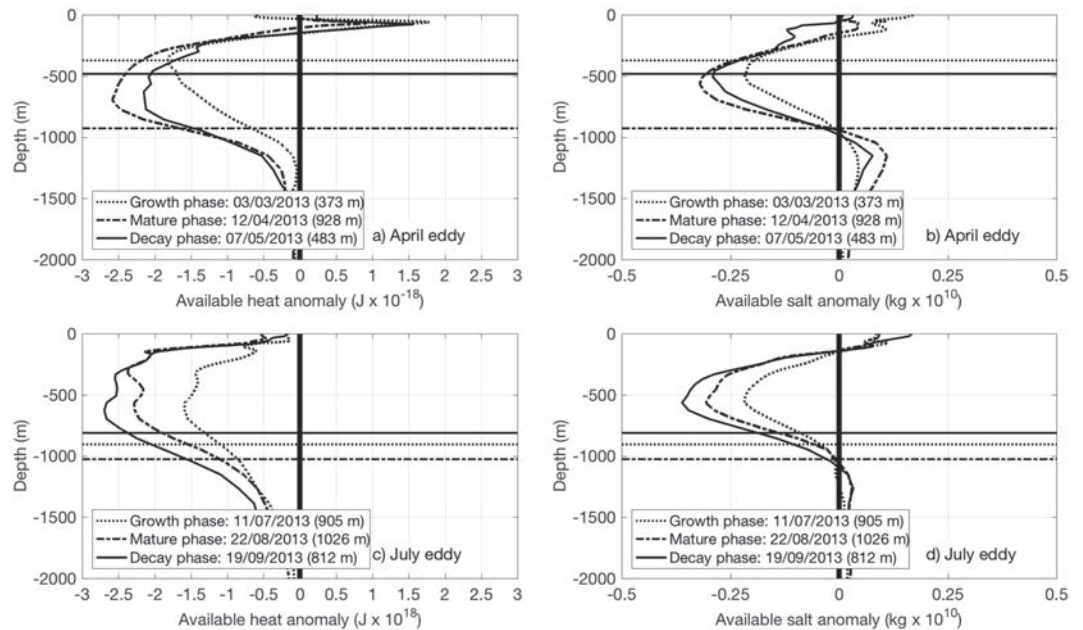


**Figure 12.** (a,c) Available heat anomaly and (b,d) available salt anomaly of the April and July eddies, respectively, for the eddy growth (black line), mature (blue line), and decay (red line) phases on the same selected dates as shown in Figures 9- 11. See legend for dates and trapped water depth.

The vertical distribution of available heat (AHA) and salt anomaly (ASA) contents is shown in Figure 12 following the growth, mature, and decay phases of each eddy. The structure of AHA and ASA for both eddies was similar with a single negative maximum subsurface centered around 400–700 and 500 m, respectively. Near the surface, a shallow positive anomaly in ASA occupied the upper 100 m of the water column for both the April and July eddies ASA, while the same applied for the AHA of the April eddy (Figures 12a, 12b, and 12d).

For the April eddy, an increase in AHA and ASA occurred from the growth to the mature phase, followed by a decrease from the mature to the decay phase. Differently, this latter decrease from the mature to the decay phase was absent for the July eddy, and instead, both AHA and ASA increased. We attribute this to the larger eddy radius exhibited by the July eddy during the date selected within its decay phase, as compared to its mature phase (Table 3). The mean vertically integrated AHA (ASA) of the April eddy was  $-58.8 \times 10^{18} \pm 65.1 \times 10^{18}$  J ( $-145.5 \times 10^{10} \pm 158.8 \times 10^{10}$  kg), and the July eddy was  $-151.7 \times 10^{18} \pm 83.7 \times 10^{18}$  J ( $-336.7 \times 10^{10} \pm 189.6 \times 10^{10}$  kg). We find these averaged estimates of total AHA and ASA (Table 3) larger than those found for cyclonic eddies in the Peru-Chile Current System ( $-5.9 \times 10^{18}$  J and  $-14.7 \times 10^{10}$  kg, respectively; Chaigneau et al. 2011) and in the Western and Eastern Indian Ocean for subsurface cyclonic eddies ( $-5.1 \times 10^{18}$  J and  $-25.6 \times 10^{10}$  kg; Dilmahamod et al. 2018). However, we must also note that estimates in these previous works are based on smoother vertical structures of the eddies since they were constructed from averaging Argo profiles over large areas to provide climatological views. It is likely expected that estimates for nonclimatological eddies will present and carry much larger anomalies given then individual eddies can display peak radius that will consequently increase the heat and salt anomaly contents. Furthermore, trapping depths in Chaigneau et al. (2011) and Dilmahamod et al. (2018) are calculated from geostrophic velocities assuming a level of no motion at a given depth. This might also lead to some underestimation when computing the nonlinearity with depth, resulting in shallower trapping depths for vertical integration of the total AHA and ASA. While in our study we use absolute model velocities, and these might be leading, on the other hand, to some overestimation of our trapping depths (and therefore of AHA and ASA).

Lastly, estimates of heat and freshwater fluxes as the eddies evolved across the southern Mozambique Channel allow us to understand better how these fluxes vary in time along the eddy lifespan and to what extent these will eventually reach and enter the Agulhas Current system (Table 3). Heat and freshwater fluxes of the April (July) eddy vary from  $-0.02$  PW ( $-0.07$  PW) and  $0.003$  Sv ( $0.04$  Sv) during the growth phase to  $-0.1$  PW ( $-0.2$  PW) and  $0.09$  Sv ( $0.14$  Sv) during the mature phase and  $-0.04$  PW ( $-0.2$  PW) and  $0.04$  Sv ( $0.10$  Sv) toward the decay phase. We observe for both eddies, peak heat and freshwater fluxes were reached during the growth phase, except for the July eddy which retains high heat fluxes also during the decay phase. The magnitude of the heat and salt fluxes were up to 1 order of magnitude higher during the mature phase than during the growth phase, occasionally decreasing toward a lower order of magnitude during the decay phase, as it occurs for heat fluxes of the April eddy. These results highlight the importance of studies characterizing the Lagrangian evolution of cyclonic eddies in the southern Mozambique Channel to properly assess their actual contribution as cool and freshwater source waters to the Agulhas Current.

Interestingly, estimates of heat fluxes driven by Madagascar cyclonic eddies approached values reported for Agulhas Rings (anticyclonic eddies) using Argo floats and satellite data reaching up to  $0.07$  PW (Souza et al., 2011); whereas freshwater fluxes driven by the April and July eddies fall within the same order of magnitude as those reported for surface and subsurface cyclonic eddies in the South Indian Ocean, which ranged along  $-0.4$ ,  $-0.02$ , and  $0.8$  Sv (Dilmahamod et al., 2018).

Our analyses of the Lagrangian evolution of Madagascar cyclonic eddies show Madagascar cyclonic eddies continuously change over their lifespan, which will have impacts on their potential contributions to the western boundary current system. In this regard, our study is, to the best of our knowledge, the first one on attempting such an approach, providing a quantitative description of the time-evolving changes experienced by the available heat and salt anomaly contents, and fluxes, that ultimately will feed into the Agulhas Current.

## 4. Concluding Remarks

### 4.1. Summary and Conclusions

This paper has characterized for the first time the 3-D Lagrangian evolution of two nonconcomitant Madagascar cyclonic eddies based on ad hoc Argo experiments undertaken in April and July 2013. The set of Argo floats were configured to measure temperature and salinity at high temporal resolutions (daily and five-daily experiments) and at varying park depths (300, 500, 650, and 1,000 m) to test their retention within the eddy dynamics. We complemented these in situ measurements with altimetry data and the output of an eddy-permitting ( $1/4^\circ$ ) ocean general circulation model (GLORYS2v4). Statistics for near-surface eddy properties were derived from application of an eddy detection and tracking algorithm (Penven et al., 2005; Halo, Penven, et al., 2014) to both altimetry and model data. The agreement among the complementary data sources reveals a number of insightful features.

The April and July eddies propagated westward from southwest Madagascar, where the SEMC separates from the continental shelf, with a moderate poleward deflection. After a propagation of 130–137 days ( $\sim 5$  months), the eddies interact with the Agulhas Current at the KwaZulu-Natal Bight. The mean propagation speed of the April and July eddies was high, 13–15  $\text{cm s}^{-1}$ , likely enhanced through advection of the eddies in the southern Mozambique Channel by favoring strong background currents. These propagation speeds are about 2 times the phase speed of nondispersive baroclinic Rossby waves for the range of latitude of Madagascar eddies (5–6  $\text{cm s}^{-1}$  at 25–30° S), exceeding the prediction from theories for nonlinear vortices (Chelton et al., 2011; Cushman-Roisin, 1994; McWilliams & Flierl, 1979).

As long-lived mesoscales features, the observed April and July Madagascar eddies evolved in time, and over space, through three well-defined phases. Along its growth phase, the eddies increased in radius from relatively small initial sizes toward a mature stage, where the eddy radius' remained nearly stable over time. The mature stage ended when the eddies started to decrease and approached their initial size along the so-called, decay phase. The time-varying relationship between the eddy radius, amplitude, and rotational speed was tight for both eddies, following each other in parallel when the eddies propagated southwestward without complex interactions with other mesoscales features and/or physical boundaries. Generally, the observed July eddy presented a larger radius (89 km), amplitude (–27 cm), and stronger rotational speeds (69  $\text{cm s}^{-1}$  than the April eddy (65 km, 16 cm, and 57  $\text{cm s}^{-1}$ , respectively). In both cases, mean rotational speeds derived from altimetry data exceeded their mean propagation speed, thus supporting their capability to transport ocean properties within their interior while traveling across the southern Mozambique Channel. The latter occurs when the ratio of the rotational speed to the propagation speed exceeds 1, indicating that the eddy is nonlinear (Chelton et al., 2011; McWilliams & Flierl, 1979; Robinson, 1983).

The analyses of water masses based on Argo floats retained within the eddies indicated Madagascar cyclonic eddies displayed the highest variability along its lifespan in the upper  $\sim 100$  m of the water column and below 900 m. We attribute changes near the surface to direct and rapid ocean-atmosphere interactions acting over the 5 months of travel. This is seen with Tropical Surface Water ( $\sigma_\theta < 25.5 \text{ kg m}^{-3}$ ; Beal et al. 2006) becoming cooler and saltier over time as the eddy propagates southwestward. The significant water mass changes occurring deeper than 900 m are here attributed to the effective trapping vertical extent of the eddies. As the floats sampling the eddy travel southwestward, we observe a progressive decrease in diluted RSW, which originated further north, and increase in AAIW, which originated further south. This is likely a response to Argo floats sampling local waters along its excursions through the water column at the time of profiling, rather than sampling water retained within the eddy from its area of origin. At 150–200 m, all eddy profiles presented a subsurface salinity maximum approaching 35.65, characteristic for Subtropical Surface Water (Gründlingh et al. 1991), and below, a rather less variable domain of South Indian Central Water between 300 and 900 m (8–14 °C, 34.6–35.4  $\text{g kg}^{-1}$ ; Emery 2001). When compared to an Argo profile sampling the Agulhas Current, the profiles within the eddy exhibit a distinctive cooler and fresher vertical distribution of ocean properties highlighted as negative temperature and salinity anomalies which extended through the water column down to 900 m, except for a relatively shallow and weak positive salinity anomaly within the upper 200 m. These negative temperature and salinity anomalies were as large as  $-2^\circ\text{C}$  (0–900 m) and  $-0.2 \text{ g kg}^{-1}$  (200–900 m), respectively, and support the potential of Madagascar cyclonic eddies to transport large temperature and salinity anomalies effectively from Madagascar to southeast Africa, from the surface down to about 900 m.

The good agreement between model and observed eddy characteristics and Lagrangian evolution allows us to extend our analyses toward model-based calculations of time-varying trapping depths and associated eddy-driven fluxes. Our results highlight the importance of studies characterizing time-evolving changes experienced by the available heat and salt anomaly contents that ultimately will feed into the Agulhas Current. In this context, we observe a distinct pattern where eddy retention increases from initially shallower values to deepest trapping depths approaching 1,000 m as the eddies grew and reached their mature stage, when rotational speeds are stronger and deep reaching. In both cases, this situation reversed toward the decay phase of the eddies, when trapping depths started to decrease following shallower strong rotational speeds. Overall, the model April (July) eddy showed mean trapping water depths of  $595 \pm 294$  m ( $914 \text{ m} \pm 107 \text{ m}$ ), volume transport about  $13.4 \pm 5.2$  Sv ( $21.2 \pm 9.1$  Sv), heat flux of  $-0.07 \pm 0.06$  PW ( $-0.2 \pm 0.09$  PW), and freshwater flux of  $0.04 \pm 0.04$  Sv ( $0.09 \pm 0.05$  Sv). These results evidence the role of Madagascar cyclonic eddies as transporters of cooled and freshened source waters into the Agulhas Current, demanding further investigation by combination of Argo dedicated experiments, remotely sensed data, and, particularly, of direct measurements of velocity at different stages of the eddy lifespan when possible. The latter is crucial to enable the evaluation of model-based estimates on time-varying eddy-driven fluxes, so we can assess the accuracy of these estimates against the real ocean.

#### 4.2. Potential of Argo-Dedicated Experiments

Results from this study complement a series of other works conducted in this region which investigate general eddy dynamics from altimetry and model data, pursuing to uncover the characterization of the eddy demography, its energetic balances, generation mechanisms, and potential links to climate variability (Dilmahamod et al., 2018; Halo, Penven, et al., 2014; Ridderinkhof et al., 2013). From a different perspective, the work in de Ruijter et al. (2004) represents to the best of our knowledge the most complete description of a Madagascar cyclonic eddy based on direct measurements of temperature, salinity, and velocity. However, these measurements characterized the eddy *only* at the time of the survey while located in the middle of the southern Mozambique Channel, being beyond the scope of their research to describe its time-varying vertical structure. Our results add to previous works new knowledge, focusing on the Lagrangian characterization of Madagascar cyclonic eddies from its generation site toward the western boundary, combining observations and model data to provide a robust view of the time-varying vertical structure and associated volume, heat, and freshwater fluxes of these eddies.

The different configurations of the Argo floats used in this study evidence the trapping capabilities of the April and July eddies, suggesting that the most suitable configuration (among tested options) to capture eddy dynamics is daily profiling with park depths between 300 and 650 m. The park depth at 1,000 m appeared to exceed the vertical extent of the April eddy, while shallower park depths resulted in floats drifting over longer periods of time within both the April and July eddies. On the other hand, the Argo trajectories revealed by daily profiling floats suggest the presence of some rapid secondary circulation patterns through the convergence/divergence of the floats toward/from the eddy core over time, which we note demand further investigation.

We are confident that the experimental design of the two Argo-dedicated experiments presented here illustrates the benefits of ad hoc Argo configurations for the study of 3-D Lagrangian eddy dynamics in combination with a “state-of-the-art” ocean model and remotely sensed data. No single experiment will likely fit all regions of mesoscale eddy turbulence, and Argo floats were never designed to answer all the questions posed by the oceanographic community (Morris & Lamont, 2019). However, dedicated experiments like these are valuable to be complemented with other data sources, validating further models and enabling a better understanding of the subsurface Lagrangian evolution of eddies not easily surveyed at different stages of their lifespan using research vessels.

#### References

- Argo (2000). Argo float data and metadata from Global Data Assembly Centre (Argo GDAC). *SEANOE*. <https://doi.org/10.17882/42182>
- Barceló-Llull, B., Sangrà, P., Pallàs-Sanz, E., Barton, E., Estrada-Allis, S., Martínez-Marrero, A., et al. et al. (2017). Anatomy of a subtropical intrathermocline eddy. *Deep-Sea Research Part I*, *124*, 126–139.
- Barlow, R., Lamont, T., Gibberd, M.-J., Airs, R., Jacobs, L., & Britz, K. (2017). Phytoplankton communities and acclimation in a cyclonic eddy in the southwest Indian Ocean. *Deep-Sea Research Part I*, *124*, 18–30. <https://doi.org/10.1016/j.dsr.2017.03.013>
- Beal, L., Chereskin, T., Lenn, Y., & Elipot, S. (2006). The sources and mixing characteristics of the Agulhas Current. *Journal of Physical Oceanography*, *36*(11), 2060–2074.

#### Acknowledgments

The authors would like to thank Woods Hole Oceanographic Institution and the U.K. MetOffice for donation of Argo floats. The authors would like to acknowledge the Captain, Officers and crew onboard the RV *Algoa* for assisting with deployments, and the science teams of the two cruises, NIOZ and ACEP, for their assistance. The authors would like to thank the two anonymous reviewers of this manuscript for the valuable assistance in the refinement of this manuscript. T. M. was supported by the South African Environmental Observation Network (SAEON), Egagasini Node, and the Oceanography Department of the University of Cape Town (UCT). All Argo data were collected and made freely available by the International Argo Program and the national programs that contribute to it (<http://www.argo.ucsd.edu> and <http://argo.jcommops.org>; (Argo, 2000)). The Argo program is part of the Global Ocean Observing System. The reanalysis model product used for this work is available for download from Copernicus (<http://marine.copernicus.eu>).

- Beal, L., de Ruijter, W., Biastoch, A., Zahn, R., & SCOR/WCRP/IAPSO Working Group 136 (2011). On the role of the Agulhas system in ocean circulation and climate. *Nature*, *472*(7344), 429–436.
- Beron-Vera, F., Wang, Y., Olascoaga, M., Goni, G., & Haller, G. (2013). Objective detection of oceanic eddies and the Agulhas leakage. *Journal of Physical Oceanography*, *43*(7), 1426–1438.
- Cabanes, C., Grouazel, A., v.Schuckmann, K., Hamon, M., Turpin, V., Coatanoan, C., et al. et al. (2013). The CORA dataset: validation and diagnostics of in-situ ocean temperature and salinity measurements. *Ocean Science*, *9*(1), 1–18.
- Casanova-Masjoan, M., Pelegrí, J., Sangrà, P., Martínez, A., Grisolia-Santos, D., Pérez-Hernández, M., & Hernández-Guerra, A. (2017). Characteristics and evolution of an Agulhas ring. *Journal of Geophysical Research: Oceans*, *122*, 7049–7065. <https://doi.org/10.1002/2017JC012969>
- Chaigneau, A., Le Texier, M., Eldin, G., Grados, C., & Pizarro, O. (2011). Vertical structure of mesoscale eddies in the eastern South Pacific Ocean: A composite analysis from altimetry and Argo profiling floats. *Journal of Geophysical Research*, *116*, C11025. <https://doi.org/10.1029/2011jc007134>
- Chelton, D. B., Deszoeke, R. A., Schlax, M. G., El Naggar, K., & Siwertz, N. (1998). Geographical variability of the first baroclinic Rossby radius of deformation. *Journal of Physical Oceanography*, *28*(3), 433–460.
- Chelton, D. B., Gaube, P., Schlax, M. G., Early, J. J., & Samelson, R. M. (2011). The influence of nonlinear mesoscale eddies on near-surface oceanic chlorophyll. *Science*, *334*(6054), 328–332. <https://doi.org/10.1126/science.1208897>
- Cushman-Roisin, B. (1994). *Introduction to Geophysical Fluid Dynamics*. Englewood Cliffs: Prentice-Hall.
- de Ruijter, W. P. M., van Aken, H. M., Beier, E. J., Lutjeharms, J. R. E., Matano, R. P., & Schouten, M. W. (2004). Eddies and dipoles around South Madagascar: formation, pathways and large-scale impact. *Deep-Sea Research Part I*, *51*(3), 383–400.
- Dilmahamad, F., Aguiar-González, B., Penven, P., Reason, C., De Ruijter, W., Malan, N., & Hermes, J. (2018). SIDDIES Corridor: A Major East-West Pathway of Long-Lived Surface and Subsurface Eddies Crossing the Subtropical South Indian Ocean. *Journal of Geophysical Research: Oceans*, *123*, 5406–5425. <https://doi.org/10.1029/2018JC013828>
- Dong, C., McWilliams, J. C., Liu, Y., & Chen, D. (2014). Global heat and salt transports by eddy movement. *Nature Communications*, *5*.
- Duacs/AVISO. (2014). A New Version of Ssalto/Duacs Products Available in April 2014, Version 1.1, CNES. *Center National D'Études Spatiales (CNES)*.
- Emery, W. J. (2001). Water types and water masses. *Encyclopedia of Ocean Sciences*, *6*, 3179–3187.
- Gründlingh, M. L., Carter, R. A., & Stanton, R. C. (1991). Circulation and water properties of the southwest Indian Ocean. *Progress in Oceanography*, *28*(4), 305–342.
- Haller, G., & Beron-Vera, F. (2013). Coherent Lagrangian vortices: The black holes of turbulence. *Journal of Fluid Mechanics*, *731*.
- Halo, I., Backeberg, B., Penven, P., Ansoerge, I., Reason, C., & Ullgren, J. E. (2014). Eddy properties in the mozambique channel: A comparison between observations and two numerical ocean circulation models. *Deep-Sea Research Part II*, *100*, 38–53.
- Halo, I., Penven, P., Backeberg, B., Ansoerge, I., Shillington, F., & Roman, R. (2014). Mesoscale eddy variability in the southern extension of the East Madagascar Current: Seasonal cycle, energy conversion terms, and eddy mean properties. *Journal of Geophysical Research: Oceans*, *119*, 7324–7356. <https://doi.org/10.1002/2014JC009820>
- Inoue, R., Honda, M. C., Fujiki, T., Matsumoto, K., Kouketsu, S., Suga, T., & Saino, T. (2016). Western North Pacific Integrated Physical-Biogeochemical Ocean Observation Experiment (INBOX): Part 2. Biogeochemical responses to eddies and typhoons revealed from the S1 mooring and shipboard measurements. *Journal of Marine Research*, *74*(2), 71–99.
- Inoue, R., Suga, T., Kouketsu, S., Kita, T., Hosoda, S., Kobayashi, T., et al. (2016). Western north Pacific integrated physical-biogeochemical ocean observation experiment (INBOX): part 1. Specifications and chronology of the S1-INBOX floats. *Journal of Marine Research*, *74*(2), 43–69.
- Kouketsu, S., Kaneko, H., Okunishi, T., Sasaoka, K., Itoh, S., Inoue, R., & Ueno, H. (2016). Mesoscale eddy effects on temporal variability of surface chlorophyll a in the Kuroshio Extension. *Journal of Oceanography*, *72*(3), 439–451.
- Law, C., Martin, A., Liddicoat, M., Watson, A., Richards, K., & Woodward, E. (2001). A Lagrangian SF6 tracer study of an anticyclonic eddy in the North Atlantic: Patch evolution, vertical mixing and nutrient supply to the mixed layer. *Deep-Sea Research Part II*, *48*(4–5), 705–724.
- Lewis, J., Kirwan, A. Jr., & Forristall, G. (1989). Evolution of a warm-core ring in the Gulf of Mexico: Lagrangian observations. *Journal of Geophysical Research*, *94*(C6), 8163–8178.
- McWilliams, J. C., & Flierl, G. R. (1979). On the evolution of isolated non-linear vortices. *Journal of Physical Oceanography*, *9*, 1155–1182.
- Menezes, V., Phillips, H., Vianna, M., & Bindoff, N. (2016). Interannual variability of the South Indian Countercurrent. *Journal of Geophysical Research: Oceans*, *121*, 3465–3487. <https://doi.org/10.1002/2015JC011417>
- Morris, T., & Lamont, T. (2019). Using ocean robots on high-resolution profiling to capture the fast-flowing Agulhas Current. *South African Journal of Science*, *115*(1–2), 9–11.
- Nauw, J. J., van Aken, H. M., Webb, A., Lutjeharms, J. R. E., & de Ruijter, W. P. M. (2008). Observations of the southern East Madagascar Current and undercurrent and countercurrent system. *Journal of Geophysical Research*, *113*, C08006. <https://doi.org/10.1029/2007JC004639>
- Ning, J., Xu, Q., Zhang, H., Wang, T., & Fan, K. (2019). Impact of Cyclonic Ocean Eddies on Upper Ocean Thermodynamic Response to Typhoon Soudelor. *Remote Sensing*, *11*(8), 938.
- Noyon, M., Morris, T., Walker, D., & Huggett, J. (2018). Plankton distribution within a young cyclonic eddy off south-western Madagascar. *Deep-Sea Research Part II*.
- Okubo, A. (1970). Horizontal dispersion of floatable particles in the vicinity of velocity singularities such as convergences. *Deep Sea Research and Oceanographic Abstracts*, *17*(3), 445–454. [https://doi.org/10.1016/0011-7471\(70\)90059-8](https://doi.org/10.1016/0011-7471(70)90059-8)
- Pegliasco, C., Chaigneau, A., & Morrow, R. (2015). Main eddy vertical structures observed in the four major Eastern Boundary Upwelling Systems. *Journal of Geophysical Research: Oceans*, *120*, 6008–6033. <https://doi.org/10.1002/2015JC010950>
- Penven, P., Echevin, V., Pasapera, J., Colas, F., & Tam, J. (2005). Average circulation, seasonal cycle, and mesoscale dynamics of the Peru Current System: A modeling approach. *Journal of Geophysical Research*, *110*, C10021. <https://doi.org/10.1029/2005JC002945>
- Pérez, J. (2003). Evolution of the open-sea eddy ALGERS'98 in the Algerian Basin with Lagrangian trajectories and remote sensing observations. *Journal of Marine Systems*, *43*(3–4), 105–131.
- Ponsoni, L., Aguiar-González, B., Ridderinkhof, H., & Maas, L. (2016). The East Madagascar Current: Volume transport and variability based on long-term observations. *Journal of Physical Oceanography*, *46*(4), 1045–1065.
- Quartly, G., Buck, J., Srokosz, M., & Coward, A. (2006). Eddies around Madagascar – The retroreflection re-considered. *Journal of Marine Systems*, *63*(3), 115–129.
- Quartly, G. D., & Srokosz, M. A. (2004). Eddies in the southern Mozambique Channel. *Deep-Sea Research Part II*, *51*(1–3), 69–83.

- Ramanantsoa, J., Penven, P., Rouault, M., & Gula, J. (2018). Coastal upwelling south of Madagascar: Temporal and spatial variability. *Journal of Marine Systems*, 178, 29–37.
- Ramanantsoa, J., Penven, P., Krug, M., Gula, J., & Rouault, M. (2018). Uncovering a new current: The Southwest Madagascar coastal current. *Geophysical Research Letters*, 45, 1930–1938. <https://doi.org/10.1002/2017GL075900>
- Ridderinkhof, W., Le Bars, D., Heydt, A. S., & de Ruijter, W. P. M. (2013). Dipoles of the south east Madagascar Current. *Geophysical Research Letters*, 40, 558–562. <https://doi.org/10.1002/grl.50157>
- Riser, S. C., Freeland, H. J., Roemmich, D., Wijffels, S., Troisi, A., Belbéoch, M., et al. et al. (2016). Fifteen years of ocean observations with the global Argo array. *Nature Climate Change*, 6(2), 145.
- Robinson, A. R. (1983). Overview and summary of eddy science. In A. R. Robinson (Ed.), *Eddies in marine science* (pp. 3–15). ISBN 978-3-642-69003-7.
- Samelson, R. M., Schlax, M. G., & Chelton, D. B. (2014). Randomness, symmetry, and scaling of mesoscale eddy life cycles. *Journal of Physical Oceanography*, 44(3), 1012–1029.
- Sangrà, P., Auladell, M., Marrero-Díaz, A., Pelegrí, J. L., Fraile-Nuez, E., Rodríguez-Santana, A., et al. (2007). On the nature of oceanic eddies shed by the Island of Gran Canaria. *Deep-Sea Research Part I*, 54(5), 687–709.
- Sangrà, P., Pelegrí, J. L., Hernández-Guerra, A., Arregui, I., Martín, J. M., Marrero-Díaz, A., et al. (2005). Life history of an anticyclonic eddy. *Journal of Geophysical Research*, 110, C03021. <https://doi.org/10.1029/2004JC002526>
- Schouten, M. W., de Ruijter, W. P. M., & van Leeuwen, P. J. (2002). Upstream control of Agulhas Ring shedding. *Journal of Geophysical Research*, 107(C8), 3109. <https://doi.org/10.1029/2001JC000804>
- Siedler, G., Rouault, M., Biastoch, A., Backeberg, B., Reason, C. J. C., & Lutjeharms, J. R. E. (2009). Modes of the southern extension of the East Madagascar Current. *Journal of Geophysical Research*, 114, C01005. <https://doi.org/10.1029/2008JC004921>
- Souza, J. M. A. C., de Boyer Montégut, C., Cabanes, C., & Klein, P. (2011). Estimation of the Agulhas Ring impacts on meridional heat fluxes and transport using ARGO floats and satellite data. *Geophysical Research Letters*, 38, L21602. <https://doi.org/10.1029/2011GL049359>
- Van Aken, H., Van Veldhoven, A., Veth, C., De Ruijter, W., Van Leeuwen, P., Drijfhout, S., et al. (2003). Observations of a young Agulhas Ring, Astrid, during MARE in March 2000. *Deep-Sea Research Part II*, 50(1), 167–195.
- Weiss, J. (1991). The dynamics of enstrophy transfer in two-dimensional hydrodynamics. *Physica D: Nonlinear Phenomena*, 48(2–3), 273–294.
- Zhang, W.-Z., Xue, H., Chai, F., & Ni, Q. (2015). Dynamical processes within an anticyclonic eddy revealed from Argo floats. *Geophysical Research Letters*, 42, 2342–2350. <https://doi.org/10.1002/2015GL063120>
- Zhang, Z., Li, P., Xu, L., Li, C., Zhao, W., Tian, J., & Qu, T. (2015). Subthermocline eddies observed by rapid-sampling Argo floats in the subtropical northwestern Pacific Ocean in Spring 2014. *Geophysical Research Letters*, 42, 6438–6445. <https://doi.org/10.1002/2015GL064601>